

Spitzer and *Herschel* studies of dust in supernova remnants in the Small Magellanic Cloud

Mikako Matsuura,^{1*} Victoria Ayley,¹ Hannah Chawner,^{1,2} M.D. Filipović,³
Warren Reid,^{3,4,5} F.D. Priestley,¹ Andy Rigby,¹ M.J. Barlow,⁶ Haley E. Gomez,¹

¹*School of Physics and Astronomy, Cardiff University, The Parade, Cardiff CF24 3AA, UK*

²*School of Chemistry, University of Bristol, Queens Road, Bristol, BS8 1QU, UK*

³*Western Sydney University, Locked Bag 1797, Penrith South DC, NSW 2751, Australia*

⁴*Department of Physics, Macquarie University, Sydney, NSW 2109, Australia*

⁵*Observatory Hill Waitoki, 130 Dormer Rd, RD2 Helensville, 0875, New Zealand*

⁶*Department of Physics and Astronomy, University College London, Gower Street, London WC1E 6BT, UK*

Accepted XXX. Received YYY; in original form ZZZ

ABSTRACT

With the entire Small Magellanic Cloud (SMC) mapped by the *Spitzer Space Telescope* and *Herschel Space Observatory*, we were able to search 8–250 μm images in order to identify infrared (IR) emission associated with SMC supernova remnants (SNRs). A valid detection had to correspond with known X-ray, H α and radio emission from the SNRs. From the 24 known SNRs, we made 5 positive detections with another 5 possible detections. Two detections are associated with pulsars or pulsar wind nebula, and another three detections are part of the extended nebulous emission from the SNRs. We modelled dust emission where fast moving electrons are predicted to collide and heat dust grains which then radiate in IR. With known distance ($62.44 \pm 0.47\text{kpc}$), measured SNR sizes, electron densities, temperatures from X-ray emission as well as hydrogen densities, the modelling of SMC SNRs is straightforward.

If the higher range of hydrogen and electron densities were to be accepted, we would expect almost all SMC SNRs to be detected in the IR, at least at 24 μm , but the actual detection rate is only 25 %. One possible and common explanation for this discrepancy is that small grains have been destroyed by the SNRs shockwave. However, within the uncertainties of hydrogen and electron densities, we find that infrared dust emission can be explained reasonably well, without invoking dust destruction. There is no conclusive evidence that SNRs destroy swept-up ISM dust.

Key words: ISM: supernova remnants – shock waves – (ISM:) dust, extinction, – ISM: individual objects: DEM S103, NGC 346, ITK 25 — galaxies: individual objects: Small Magellanic Cloud

1 INTRODUCTION

Dust grains are small particles made of minerals, and are typically composed of silicon or carbon, together with other metals, such as magnesium, oxygen and iron. The detection of a vast amount of dust grains ($> 10^8 M_{\odot}$) in the interstellar medium (ISM) of galaxies within the Local Universe and out to high redshifts (e.g. Bertoldi et al. 2003; Watson et al. 2015; Laporte et al. 2017) triggered a debate over how these dust grains could have been acquired in cosmic time. In the Local Universe, asymptotic giant branch (AGB) stars, the late phase of low- and intermediate-mass stars may be able to account for a substantial amount of this dust mass (Gehrz 1989; Dwek 1998; Matsuura et al. 2009, 2013), with a possible contribu-

tion from ISM grain growth (Tielens 2010; Galliano et al. 2018). However, the evolutionary timescale for low- and intermediate-mass stars (Morgan & Edmunds 2003) and the ISM grain growth (Ferrara & Peroux 2021) might be too slow to achieve the large amounts of dust seen in high redshift galaxies. Supernovae (SNe) have been suggested as an alternative and additional source of dust in the ISM of galaxies (e.g. Morgan & Edmunds 2003; Maiolino et al. 2004; Matsuura et al. 2009; Cherchneff & Dwek 2010; Hjorth et al. 2013).

Although SNe eject newly synthesised heavy elements into the ISM, questions remain over the proportion of the metals that condense into dust grains, and how much of the SN and ambient ISM dust can survive SN shocks (e.g. Nozawa et al. 2003; Schneider et al. 2004; Cherchneff & Dwek 2010; Sarangi & Cherchneff 2015). Chemical modelling predicts that a SN may produce approximately 0.1–1 M_{\odot} of dust (Dwek & Cherchneff 2011; Sarangi & Cherch-

* E-mail: matsuuram@cardiff.ac.uk (MM)

neff 2015), however, their survival rate after encountering reverse shocks is currently predicted as anywhere between 1% and 90% (e.g. Micelotta et al. 2016, 2018; Kirchschrager et al. 2019), a large uncertainty. Moreover, while SNRs expand at speeds ranging between a few hundred and a few thousand km s^{-1} , the forward shock can destroy existing ambient ISM dust (McKee & Hollenbach 1980; Jones et al. 1996; Bocchio et al. 2014; Micelotta et al. 2018). Even though dust grains may be produced by AGB stars and SN ejecta, the destruction of dust by forward shocks can be so efficient as to lower or eliminate the total ISM dust budget. This has led some to conclude that the ISM of galaxies might not be able to maintain a large amount of dust grains (e.g. Jones et al. 1996; Michałowski et al. 2010).

While modelling predicts both production and destruction of dust by SNe and SNRs, recent observations reveal that indeed SNe can produce a substantial mass of dust in their ejecta. Amongst remnants of core-collapsed SNe, a large amount ($\sim 0.1\text{--}1 M_{\odot}$) of dust has been detected, including SN 1987A (Matsuura et al. 2011, 2015; Wesson et al. 2015), Cassiopeia A (Rho et al. 2008; Barlow et al. 2010; De Looze et al. 2017; Niculescu-Duvaz et al. 2021), Crab Nebula (Gomez et al. 2012b; Temim & Dwek 2013; De Looze et al. 2019). Additionally, there are reports of significant quantities of dust in SMC 1E 0102–7219 (SNR J0104.0–7202) (Stanimirović et al. 2005; Sandstrom et al. 2009). However, challenges remain regarding how to measure the amount of dust that can survive passage through the reverse shock, its wake and the follow-up radiation from the SN. These SNRs with dust measurements are relatively young, estimated at $\sim 30\text{--}1000$ years only. In order to evaluate the true impact of SN shocks on dust destruction, the ageing effects on dust should be examined using older SNRs. Somehow among older SNRs, those with pulsar wind nebulae (PWNe), whose ejecta are heated by radiation from the neutron stars (Chevalier 1977; Chevalier & Fransson 1992; Hester 2008) have been frequently reported to have a substantial quantity of dust, including G54.1+0.3 (Temim et al. 2017; Rho et al. 2018), G11.2–0.3, G21.5–0.9, G29.7–0.3 (Chawner et al. 2019), SNR 0540–69.3 (Lundqvist et al. 2020). It is still yet unknown why the detection rate of ejecta dust in PWNe appears to be higher than in general SNRs. It might be because the presence of a heating source, pulsars, warm the ejecta, thereby allowing the PWN dust to stand out against the cooler ISM dust (Chawner et al. 2019).

The dust destruction rate by forward shocks is even more difficult to estimate. Lakicevic et al. (2015) estimated infrared emission towards Large Magellanic Cloud (LMC) SNRs and surrounding ISM, suggesting ISM dust density is lower towards SNRs. However, the reduced ISM dust density towards the SNRs could be artificially caused by hotter SNR dust emission that can hide a larger amount of colder ISM dust emission along the line of sight (Micelotta et al. 2018). The method used by Lakicevic et al. (2015) gives inconclusive results for the SNR dust destruction rate. Temim et al. (2015) estimated the dust destruction rate in the LMC, however, the actual destruction rate still relies on the theoretical dust destruction rate. Therefore, measuring the dust destruction rate is very challenging. One of the better methods to estimate the dust destruction rate is to consider the energy balance between collisional heated dust grains (by electrons) and radiation (Dwek & Arendt 1992). Since heating by electron collision and infrared radiation depends on the dust properties, including dust mass and grain size, this method can potentially inform the dust destruction rate, if mass and size of ISM dust grains prior to the shocks can be estimated or assumed. Williams et al. (2006) suggested that infrared dust emissions observed in three SNRs are consistent with collisionally

heated dust, and that the estimated dust mass is smaller than the expected SNR swept-up dust mass, hence, dust destruction is occurring. Unfortunately, there was little description of the uncertainties in the estimated dust mass, and it is unclear how accurate the dust destruction rate is. A more recent survey of Galactic and LMC SNRs found that infrared dust emission is overwhelmingly fainter than what the collisionally heated dust model predicts (Seok et al. 2013, 2015; Koo et al. 2016). This discrepancy might either be due to a lack of small dust grains, which have already been destroyed (Dwek et al. 2008), or due to dust grains that are heated by radiation, rather than by collisions (Koo et al. 2016).

To date, studies of dust in SNRs have been limited by small sample sizes. In order to increase the sample size and improve the evaluation of SNR dust emission, we conducted this search in SMC, a dwarf irregular galaxy at a distance of approximately 60 kpc (Van den Bergh 2007; Graczyk et al. 2020). Due to our viewing angle within the Galactic plane, the evaluation of infrared emission from SNRs often suffers from severe confusion with general ISM emission (Chawner et al. 2019; Chawner 2020), but viewed away from the Galactic plane, the SMC is much less prone to the ISM confusion problem. A second advantage of studying SMC SNRs is that together with the general known distance, the SMC has an estimated depth of only 4–10 kpc (Hatzidimitriou et al. 1993; Subramanian & Subramanian 2009; Graczyk et al. 2020), translating to distance uncertainties of only about 15–20% for the SNRs. This is in contrast to Galactic SNR distances, where uncertainties often amount to a few factors. Distance uncertainties propagate into the sizes and inferred dust masses of SNRs, so the distance uncertainties are an important factor in dust analysis. Thirdly, the local star-formation history has been analysed, so that the ages of SNRs may be more estimated (Lopez et al. 2014; Auchettl et al. 2019). Fourthly, there is a complete X-ray image of the SMC, which can inform the electron temperature and electron density measurements (Auchettl et al. 2019; Maggi et al. 2019). The electron temperature and density are crucial parameters for a collisionally heated dust model.

The SMC has the disadvantage of being more distant than the Milky Way, so that SNRs tend to be fainter, and have fewer expansion velocity measurements available. Above all, there are only about 25 SNRs or SNR candidates known in the SMC (Maggi et al. 2019), compared with over 250 SNRs and candidates in the Milky Way (Green 2009). Nevertheless, with electron density and temperature measurements, important in estimating the dust destruction rate, plus infrared images, we were able to conduct the following analysis of SMC SNRs.

Note that the SMC is known to have a much lower metallicity than the Milky Way or the LMC, and it has been estimated that the dust-to-gas ratio in the SMC ISM is much lower (Gordon et al. 2014).

2 SOURCE CATALOGUE

We assembled a list of known SNRs in the SMC from several references, mainly radio and X-ray surveys.

The optical $H\alpha$ and [N II] emission line surveys were originally used to find large nebulous objects in the SMC (Davies et al. 1976), but their classification as SNRs had to await the application of early radio detections. Radio surveys are effective at detecting the synchrotron radiation produced by SNRs, clearly separating them from other large nebulous objects such as HII regions. Since the year 2000, a new generation of radio surveys at the Australia Telescope Compact Array (ATCA) has led to the identification of nearly 30

SNRs and SNR candidates (e.g. Filipovic et al. 2002, 2008; Payne et al. 2007). In each case the radio brightness and spectral index were used to determine the synchrotron component.

Most SNRs stand out in the X-ray wavelength (Borkowski et al. 2006; Bozzetto et al. 2017), providing an extra means of identification. One of the first X-ray surveys of the SMC resulted in the *Chandra* Catalogue of Magellanic Cloud Supernova Remnants which listed 14 in the SMC¹. A further catalogue from Badenes et al. (2010) listed 23 remnants with X-ray and radio band detections using existing catalogues such as Filipovic et al. (2005). Most of the remnants listed by the *Chandra* Catalogue appeared in Badenes et al. (2010), apart from SNR B0044–73.4, N19, HFPK-285 and SXP-1062. The *XMM-Newton* study by Haberl et al. (2012) included the remnants catalogued by Badenes et al. (2010), while adding SXP-1062, and three new candidates, bringing the total to 30 SMC remnants. Finally, Auchettl et al. (2019) derived elemental abundances and SN types, describing whether SNRs are the result of core collapse or not. Based on elemental abundances, they eliminated some SNR candidates, leading to a total of 25 SNRs and SNR candidates. It was important that the catalogue contained celestial coordinates and sizes, so the location of the infrared-counterpart could be localised. The catalogue also contained X-ray brightness, as the plasma detected in X-rays is thought to be responsible for infrared dust emission from SNRs with shock heated gas (Dwek et al. 2008; Koo et al. 2016).

More recently, a catalogue of SMC SNRs was used to investigate SNR populations, the star-formation history, and dust destruction rates (Badenes et al. 2010; Temim et al. 2015), as well as SNR morphologies and the impact they make to their environments (Lopez et al. 2014). These catalogues laid the foundations for multi-wavelength studies of SMC SNRs spanning X-ray to radio wavelengths, leading to measurements of metallicities and estimates of progenitor star masses (Maggi et al. 2019). Maggi et al. listed *XMM*, optical and radio images of SMC SNRs, which we include as reference images to compare with *Spitzer* and *Herschel* images.

¹ https://hea-www.harvard.edu/ChandraSNR/snrcat_lmc.html

Table 1. List of SMC SNRs and SNR candidates

Name	RA	Dec	D	D. Wav.	S. Wav.	Type	Ref	Comment				
SNR J0040.9–7337	B0039–73.53	DEM S5	00h40m55s	–73d36m55s	2.5	R	RX	ABFHM				
SNR J0046.6–7307	B0044–73.4	DEM S32	00h46m41s	–73d07m55s	3.5	X	RX	CM				
=SNR J0046.6–7309			00h46m39s	–73d08m39s	2.3	R	CC	ABHM				
SNR J0047.2–7308	B0045–73.4		IKT 2	00h47m12s	–73d08m26s	1.5	X	RX	CC	ABCFHM		
SNR J0047.5–7306	B0045–73.3			00h47m29s	–73d06m01s	2.7	R	RX	AGFHM	In N19 / HII		
=SNR J0047.5–7307		NS19?	HFPK 419?	00h47m32s	–73d07m45s	4.5	X	X	C			
SNR J0048.4–7319	B0046–73.5	DEM S42E		IKT 4	00h48m25s	–73d19m24s	2.0	X	RX	Ia	ABCFHM	
SNR J0049.0–7306					00h49m00s	–73d06m17s	1	X	X	CC	H	SNR cand.
SNR J0049.1–7314	B0047–73.5	DEM S49		IKT 5	00h49m07s	–73d14m35s	2.7	R	RX	Disputed	ABCFHM	
SNR J0051.1–7321	B0049–73.6	DEM S53		IKT 6	00h51m07s	–73d21m29s	3.0	X	RX	CC	AGCFHM	
SNR J0052.6–7238	B0050–72.8	DEM S68SE			00h52m33s	–72d37m35s	5.4	X	RX		ABFHM	
=SNR J0052.9–7237		HFPK 285			00h53m01s	–72d36m52s	5.0	X	X		Cf	
SNR J0056.5–7208					00h56m30s	–72d08m12s	2.0	X	X		HM	SNR cand.
SNR J0057.7–7213					00h57m46s	–72d13m04s	3.0	X	X		HM	SNR cand.
SNR J0058.3–7218	B0056–72.5			IKT 16	00h58m16s	–72d18m05s	4.5	X	RX	CC	HFM	
SNR J0059.4–7210	B0057–72.2	DEM S103		IKT 18	00h59m25s	–72d10m10s	2.3	X	RX	CC	ABCFHM	
SNR J0100.3–7134	B0058–71.8	DEM S108			01h00m21s	–71d33m40s	3.5	R	RX		ABFHM	
SNR J0103.2–7209	B0101–72.6			IKT 21	01h03m17s	–72d09m42s	1.5	R	RX	CC	ABFHM	
SNR J0103.5–7247		HFPK 334			01h03m30s	–72d47m20s	1.5	R	RX		ABCFM	
SNR J0103.6–7201					01h03m36.5	–72d01m35s	1.5		Opt		M	
SNR J0104.0–7202	B0102–72.3	DEM S124		IKT 22	01h04m02s	–72d01m48s	1.0	X	RXOpt	I Ib	ABCFHM	
SNR J0105.1–7223	B0103–72.6	DEM S125		IKT 23	01h05m04s	–72d22m56s	3.5	X	RX	CC	ABCFHM	
SNR J0105.6–7209		DEM S128			01h05m27s	–72d10m38s	3.2	R	RX	Ia	ABFHM	
SNR J0106.2–7205	B0104–72.3			IKT 25	01h06m20s	–72d05m18s	2.5	R	RX	Disputed	ABCFHM	
SNR J0106.5–7242					01h06m32.1s	–72d42m17.0	2.58	R			M	SNR cand.
SNR J0109.7–7318					01d09m43.6s	–73d18m46s	1.75		Opt		M	SNR cand.
SNR J0127.7–7332		SXP 1062			01h27m46s	–73d32m56s	3.5	Opt	Opt	Disputed	CHM	Pulsar or HXB?
Non-SNRs?												
SNR J0047.8–7317		NS 21			00h47m48s	–73d17m27s	2.0	R	R		ABFH	SNR cand. / HII region
SNR J0051.9–7310				IKT 7	00h51m54s	–73d10m24s	1.6	X	X	CC	ABHM	XB
SNR J0114.0–7317		N83C			01h14m00s	–73d17m08s	0.5	R	R		ABHM	HII region?

Some SNRs (J0046.6–7307, J0047.5–7307 and J0052.9–7237) are listed with slightly different coordinates arising from observations made at different wavelengths, so both of them are listed after ‘=’. D: Diameter is in arcmin. D.Wav.: Wavelength used for measuring the diameter (R: radio and X: X-ray). S. Wav.: Studied wavelengths in the literature. References: A: Auchettl et al. (2019), B: Badenes et al. (2010), C: Chandra Catalogue, F: Filipovic et al. (2005), f: Filipovic et al. (2008), H: Haberl et al. (2012), M: Maggi et al. (2019) and N: Nota et al. (2006). XB: X-ray binary. HXB: high-mass X-ray binary

Table 2. Infrared detection level with properties of SNRs: abundance, age and progenitor mass, if the SNR is of core-collapse origin.

Name	IR Det	kT	EM	n_{H}	$n_{\text{H,ISM}}$	F_{24}	F_{70}	F'_{24}	F'_{70}	Age	Mass (M_{\odot})	Ref	Mass possibilities (%)
SNR J0040.9–7337	Detection	$0.65^{+0.09}_{-0.12}$	$4.01^{+0.96}_{-0.39}$	0.04	0.51	0.04	0.7	0.4	7				8–12.5 (100%)
SNR J0046.6–7307	Possible detection	$0.60^{+0.11}_{-0.11}$	$7.71^{+3.45}_{-1.64}$		1.67								>21.5 (92%); 8–12.5 (8%)
=SNR J0046.6–7309													
SNR J0047.2–7308	Unlikely detection	$0.60^{+0.04}_{-0.05}$	$13.7^{+4.87}_{-0.45}$	0.03	1.76	0.9	4.4	7.2	34				>21.5 (92%); 8–12.5 (8%)
SNR J0047.5–7306	Non detection	$0.63^{+0.25}_{-0.13}$	$5.64^{+4.87}_{-4.78}$		1.71						15–22.5	K	>21.5 (92%); 8–12.5 (8%)
=SNR J0047.5–7307													
SNR J0048.4–7319	Unlikely detection	$1.07^{+0.76}_{-0.18}$	$1.03^{+0.65}_{-0.58}$		1.89								>21.5 (59%); 12.5–21.5 (17%); 8–12.5 (24%)
SNR J0049.0–7306	Unlikely detection												
SNR J0049.1–7314	Unlikely detection	$0.52^{+0.15}_{-0.14}$	$3.16^{+3.63}_{-1.64}$		1.48								>21.5 (59%); 12.5–21.5 (17%); 8–12.5 (24%)
SNR J0051.1–7321	Unlikely detection	$0.21^{+0.01}_{-0.01}$	$171^{+22.4}_{-33.6}$	0.05	1.13	0.2	4.0	0.8	16	14000	13–15 or 15–22.5	HK	12.5–21.5 (54%); 8–12.5 (46%)
SNR J0052.6–7238	Detection	$0.38^{+0.66}_{-0.16}$	$27.4^{+308}_{-24.6}$		0.79								8–12.5 (100%)
=SNR J0052.9–7237													
SNR J0056.5–7208	Non detection												
SNR J0057.7–7213	Non detection												
SNR J0058.3–7218	Unlikely detection	$0.37^{+0.26}_{-0.09}$	$28.5^{+60.5}_{-22.1}$		0.92								
SNR J0059.4–7210	Possible detection	$0.66^{+0.03}_{-0.03}$	$25.9^{+2.37}_{-2.15}$	0.04	0.64	0.8	4.4	3.0	17	200000		N	
SNR J0100.3–7134	Non detection	$0.49^{+0.14}_{-0.16}$	$3.28^{+4.96}_{-0.99}$		0.50								>21.5 (100%)
SNR J0103.2–7209	Unlikely detection	$1.0^{+0.33}_{-0.20}$	$1.97^{+0.45}_{-0.40}$	0.03	0.89	0.3	1.5	2.6	15				>21.5 (92%); 8–12.5 (8%)
SNR J0103.5–7247	Possible detection	1.3	$0.93^{+0.45}_{-0.35}$		0.70								Ia
SNR J0103.6–7201	Possible detection												
SNR J0104.0–7202	Detection				0.85					2050	<15 or 25–35	BKX	>21.5 (49%); 12.5–21.5 (20%); 8–12.5 (31%)
SNR J0105.1–7223	Non detection	$0.19^{+0.01}_{-0.01}$	$448^{+51.7}_{-51.7}$	0.06	0.67	0.4	6.5	0.7	12	18000	~18 or 15–22.5	KP	8–12.5 (100%)
SNR J0105.6–7209	Possible detection	$0.68^{+0.20}_{-0.11}$	$4.44^{+1.72}_{-0.78}$	0.05	0.91	0.02	0.6	0.5	12				>21.5 (76%); 12.5–21.5 (15%); 8–12.5 (9%)
SNR J0106.2–7205	Detection	$0.72^{+0.07}_{-0.08}$	$9.95^{+1.59}_{-1.51}$	0.04	0.90	0.2	1.8	2	18	17600	18–25 or 25 ^a	L	>21.5 (76%); 12.5–21.5 (15%); 8–12.5 (9%)
SNR J0106.5–7242	Non detection												
SNR J0109.7–7318	Non detection												
SNR J0127.7–7332	Detection	$0.19^{+0.02}_{-0.01}$	$25.8^{+19.1}_{-12.7}$										
Non-SNRs?													
SNR J0047.8–7317	Possible detection												
SNR J0051.9–7310	Unlikely detection												
SNR J0114.0–7317	Non detection												>21.5 (100%)

Infrared (IR) detection (either *Spitzer* or *Herschel*, or both). kT (keV): electron temperature estimated from X-ray spectra (Maggi et al. 2019), EM: emission measure (Maggi et al. 2019), n_{H} : hydrogen density estimated from EM. $n_{\text{H,ISM}}$: average hydrogen density in the line of sight, estimated from HI line (Temim et al. 2015). F_{24} and F_{70} : predicted surface brightnesses (MJy sterad^{-1}) of a SNR at 24 and 70 μm , using n_{H} (Sect. 5.1). F'_{24} and F'_{70} : the same as F_{24} and F_{70} , but using $n_{\text{H,ISM}}$. Age: estimated age in years; Mass: estimated progenitor mass in M_{\odot} ; Ref: reference; Mass possibilities: estimated progenitor mass (M_{\odot}) from star-formation history at the SNR location and the probabilities (%) of the given mass (Auchettl et al. 2019). ^a: There is a dispute as to whether SNR J0106.2–7205 is of core collapse or type Ia origin. The estimated mass here is based on the core collapse case. References: B: Blair et al. (2000) H: Hendrick et al. (2005), L: Lopez et al. (2014), K: Katsuda et al. (2018), P: Park et al. (2003), X: Xi et al. (2019),

3 SPITZER, HERSCHEL AND ANCILLARY DATA

The *Spitzer Space Telescope* (Werner et al. 2004) and *Herschel Space Observatory* (Pilbratt et al. 2010) surveyed the SMC at mid- and far-infrared wavelengths. The Spitzer imaging survey of the SMC project, SAGE-SMC (Gordon et al. 2011), used in total 7 bands, IRAC 3.6, 4.5, 5.8 and 8.0 μm (Fazio et al. 2004) and MIPS 24, 70 and 160 μm (Rieke et al. 2004). The HERITAGE is the *Herschel* Magellanic Cloud survey (Meixner et al. 2010, 2013) at 100, 160 μm from PACS (Poglitsch et al. 2010), and 250, 350 and 500 μm from SPIRE (Griffin et al. 2010). The HERITAGE surveyed the Magellanic Clouds with PACS and SPIRE Parallel mode, which has a choice of only two PACS filters (100, 160 μm) out of three available filters, and whose fast scan speed limits its PACS spatial sampling rate and sensitivities. For some SMC SNRs, dedicated *Herschel* pointed observations are available (Proposal IDs: OT1_ksimon01_1 and OT2_ksandstr_3), and these observations have better spatial sampling and better sensitivities. HERITAGE included these pointed observations in the data reduction. In the case of SNR J0104.0–7202 (or 1E102.2–7219) from Proposal ID of OT2_ksandstr_3, an additional PACS 70 μm image had been taken (Ludwig et al. 2018). The PACS 70 μm image has higher angular resolution (FWHM of the point spread function is 5.46"×5.76" at medium scan rate according to the PACS Observer Manual) than the *Spitzer* MIPS 18" resolution at 70 μm , so that we used PACS 70 μm images. Filter bands and sensitivities are summarised in Table 3.

From all available Spitzer/IRAC bands, we give more weight to IRAC 8.0 μm , as SNRs tend to stand out most at 8.0 μm compared to other IRAC bands (Reach et al. 2006). IRAC 8.0 μm represents [Ar II], H₂ lines and synchrotron emission, with a possible contribution of dust emission. The SNR emission at MIPS 24 μm band is usually dominated by dust emission (Pinheiro Gonçalves et al. 2011), however, lines such as 26 μm [Fe II] and [O IV] (Bouchet et al. 2006; Rho et al. 2008; Sandstrom et al. 2009) might contribute to the brightness.

Although both filters are called ‘70 μm band’, the MIPS 70 μm band covers 61 to 80 μm , while the PACS 70 μm band covers a slightly different 60–85 μm . The PACS 100 μm band ranges from 85 to 125 μm . Flux from SNRs at these bands are dominated by dust emission in general, as found in grey body profiles in the far-infrared regime (Gomez et al. 2012b; Chawner et al. 2019). Contaminations of lines (63 μm [O I] and 88 μm [O III]) are mostly negligible: for example, the fraction of line contaminations are estimated at 5% and 6%–13% at PACS 70 and 100 μm bands respectively for the Crab Nebula (Gomez et al. 2012b), and only 6% and 2% for Galactic SNR Kes 75 (Temim et al. 2019).

X-ray images are taken from the Chandra Catalogue of Magellanic Cloud Supernova Remnants, if available, otherwise the *XMM-Newton* survey of the Magellanic Clouds (Haberl et al. 2012) is used. Unless otherwise stated in Figure captions, X-ray images shown are from *XMM-Newton* 0.2–1.0 keV, a band that indicates the thermal spectrum SNRs, with some contributions from lines, such as oxygen and Fe (Maggi et al. 2019). We use these *XMM-Newton* images of SNRs, having previously been studied by Haberl et al. (2012) and Maggi et al. (2019), to guide our astrometry for related emission in infrared wavelengths.

Optical H α , [O III] 5007 Å and [S II] 6716 and 6731 Å images from the Magellanic Cloud Emission Line Survey (MCELS) (Smith et al. 2000) are also used to identify the structure of SNRs when combined with the infrared images. MCELS surveyed the Magellanic Clouds, with sampling of 2.4 arcsec pixels and 3–4 arcsec resolution (Smith et al. 2000) and has already been used to identify

emission from SNRs, planetary nebula, and HII regions (e.g. Reid 2014). The MCELS images have also been used to identify optical counterparts of SNRs detected in X-ray and radio bands (Maggi et al. 2019). Importantly, these images can also reveal the locations of HII regions, thereby helping to distinguish SNRs from HII regions in our infrared images.

Radio continuum images of the SMC that we used are from the Australian Square Kilometre Array Pathfinder (ASKAP) (Joseph et al. 2019), that covered at two bands at 960 MHz and 1320 MHz. The beam sizes are 30"×30" and 16.3"×15.1", and the sensitivities are 186 and 165 μJy per beam and respectively. We used a 1320 MHz image to trace the synchrotron radiation from SNRs.

4 DETECTIONS OF INFRARED EMISSION FROM SUPERNOVA REMNANTS

Following the classification of detection levels from Reach et al. (2006), Pinheiro Gonçalves et al. (2011) and Chawner et al. (2019, 2020), we classified Infrared (IR) detection (either *Spitzer* or both *Spitzer* and *Herschel*) from SNRs into four levels, described in Table 4. The detection levels of individual SNRs are summarised in Table 1. This should refer to Table 2.

4.1 Descriptions of Individual SNRs

We present *Spitzer* and *Herschel* images of SNRs and their surroundings, with comparison X-ray, optical and radio images. The default X-ray images are *XMM-Newton* 0.2–1.0 keV images, but occasionally other bands (1.0–2.0 or 2.0–4.5 keV) or *Chandra* images are used. The optical images are mostly H α but an [O III] image is used for SNR J0104.0–7202, as this oxygen-rich SNR allows more detail to be seen in [O III]. The default radio images are 1320 MHz but some figures display at 960 MHz. All alternations of the selected bands are mentioned in the figure captions.

In this Section, only detections and possible detections (Table 2) are included, while unlikely, non-detections and SNR candidates/non-SNRs are included in on-line material (Sections A1 and A2).

4.1.1 SNR J00409–7337, B0039–72.53, DEM S5: detection

A pulsar-powered bow shock was discovered in SNR J00409–7337 (Alsaberi et al. 2019), using the Australia Telescope Compact Array (ATAC) at 2048 MHz and IRAC 8 μm . This pulsar is a bright point source in the 1320 MHz image (Fig. 1.i). The bow shock was detected as faint filaments both north and south of the pulsar in H α and IRAC 8 μm images, as reported by Alsaberi et al. (2019). Based on the IRAC mid-IR emission diagnostic, this bow shock is thought to trace shock-excited molecular hydrogen lines (Alsaberi et al. 2019).

The brightest discrete region of the bow shock in H α (Fig. 1.h) is also the brightest region in the 8 μm image, however, it is not particularly strong at 24 and 70 μm . The detection of a strong X-ray point source at this same position and the presence of the pulsar or PWN was suggested from X-ray spectra Alsaberi et al. (2019). Presently the source of this IR emission is unclear, either pulsar/PWN or part of the bow shock.

The most prominent feature of the SNR is the filamentary arc extending north/south and curving around at each end. This can clearly be seen to correlate between the H α and IRAC 8 μm images.

Table 3. The SMC surveys used in this study

Project	Band	Res (")	Sensitivity	Ref
MCLES	H α	3–4	3×10^{-17} erg cm $^{-2}$ s $^{-1}$ arcsec $^{-2}$	S
	[S II]	3–4		S
	[O III]	3–4		S
Spitzer	3.6 μ m	2	0.04 MJy sr $^{-1}$ (5σ)	B
	4.5 μ m	2	0.05 MJy sr $^{-1}$ (5σ)	B
	5.8 μ m	2	0.2 MJy sr $^{-1}$ (5σ)	B
	8.0 μ m	2	~ 0.1 MJy sr $^{-1}$ (5σ)	G
	24 μ m	6	0.3 MJy sr $^{-1}$ (5σ)	G
	70 μ m	18	2.5 MJy sr $^{-1}$ (5σ)	G
Herschel	70 μ m	5.2–5.8 ¹	²	
	100 μ m	6.7 \times 6.9	85–90 MJy sr $^{-1}$ (10σ) ³	M
	160 μ m	10.7 \times 12.1	32–50 MJy sr $^{-1}$ (10σ) ³	M
	250 μ m	18.2	6 MJy sr $^{-1}$ (10σ)	M
	350 μ m	24.9	3 MJy sr $^{-1}$ (10σ)	M
	500 μ m	36.3	2 MJy sr $^{-1}$ (10σ)	M
ASKAP	960 MHz (32 cm)	30 \times 30	186 μ Jy beam $^{-1}$ (RMS)	J
	1320 MHz (23cm)	16.3 \times 15.1	165 μ Jy beam $^{-1}$ (RMS)	J

Note: ¹: PACS angular resolutions depend on mapping scan speed, which varies. ²: PACS 70 μ m was not used by the HERITAGE project, but used for localised imaging for some dedicated area. Sensitivity varies on the projects. ³: HERITAGE sensitivities. Dedicated local mapping might have better sensitivities. References: B: Bolatto et al. (2007) Smith et al. (2000) G: Gordon et al. (2011) J: Joseph et al. (2019) M: Meixner et al. (2013) S: Smith et al. (2000)

Table 4. The description of detection levels.

Level	Description
Detection	IR emission is clearly correlated with radio or X-ray structure of a SNR and can be distinguished from ISM emission
Possible detection	IR emission in the region of the SNR, potentially related to radio or X-ray structure but confused with ISM emission
Unlikely detection	Detection of IR emission which is probably unrelated to the SNR
No detection	

Emission possibly associated with this arc is also found at 70 μ m but less so at 160 μ m.

4.1.2 SNR J0046.6–7307, B0044-73.4, DEM S32: possible detection

SNR J0046.6–7307 was initially found in an *XMM-Newton* image (Van der Heyden et al. 2004) and is a candidate core-collapse SNR (Van der Heyden et al. 2004). Together with SNR J0047.2–7308 (IKT 2) and SNR J0047.5–7306, it is one of the three SNRs located in a large complex HII region N19 (Davies et al. 1976; Maggi et al. 2019). SNR J0046.6–7307 is a shell shaped SNR, as seen in H α and the 1320 MHz radio image (Fig. 2) and is surrounded by at least eight molecular clouds (Sano et al. 2019). The bright emission found to the north of the SNR is the HII region NGC 261.

In *Spitzer* and *Herschel* images, part of the shell may be detected. The brightest part of the shell in the radio image is south-west, a position where faint emission can also be seen in the infrared images. At a minimum it is clearly detected at 8 and 24 μ m with associated emission probably detected at longer wavelengths. Since the majority of the arc comprising the shell in H α is slightly offset and a different shape to that found in 8 μ m, we prefer to label this as a “possible” detection. Fig. 3 shows an 8, 24, 70 μ m 3-color image of SNR J0046.6–7307, allowing the 8 μ m emission in south-west part of the shell to show prominently in blue, indicating relatively hotter

dust than in the surrounding ISM. In Galactic studies, swept up dust in SNRs tends to be warmer than unrelated ISM dust (Chawner et al. 2019), so it is still highly likely that this arc may be SNR related dust. However, since the potential of this feature being a part of ISM filaments can not be totally excluded, it is classified as a “possible detection”.

Additionally, there is a diffuse cloud found crossing the centre of this SNR from north-east to south-west in all infrared images. This cloud is redder than the south-west shell (Fig. 3), hence, it is probably not associated with the SNR but rather the ISM. Indeed, no emission corresponding to this cloud is found in X-ray nor radio.

The south-east part of the shell contains point sources, and at least one of them is a star detected in the H α image. Since it is much brighter at 24 μ m than 8 μ m, compared with other stars within the field, it may be either a red star or a dust-enshrouded star. If these point sources are part of molecular cloud D, according to Sano et al. (2019), which surrounds the SNR, they could be recently formed stars, triggered by the compression of the gas from the SNR.

4.1.3 SNR J0049.1–7314, B0047-73.5, DEM S49, IKT 5: unlikely detection but bow shock detected within a field

Although we list this SNR as an unlikely detection, a notable detection of a bow shock allows it to be included in this section.

This SNR shows its shell type structure in the radio image, but emission from iron-rich ejecta is found in the centre in the X-ray image, suggesting type Ia origin (Maggi et al. 2019). There is no detection of this shell in the infrared images (Fig. 4).

A crescent-shaped emission arc next to a point source is detected on the east side of the white circle in the H α and 8 μ m images (Fig. 4 h). This is a bow shock with the crescent and point source also found in the radio image. The crescent is not spatially resolved at longer wavelengths but still detected across all infrared images. Fig. 5 shows a three-colour image of the region, composed of 3.6, 5.8 and 8.0 μ m. This image clearly indicates the bow shock, as well as some nebulosity extending towards the north-east.

The source of this bow shock is most likely the out-

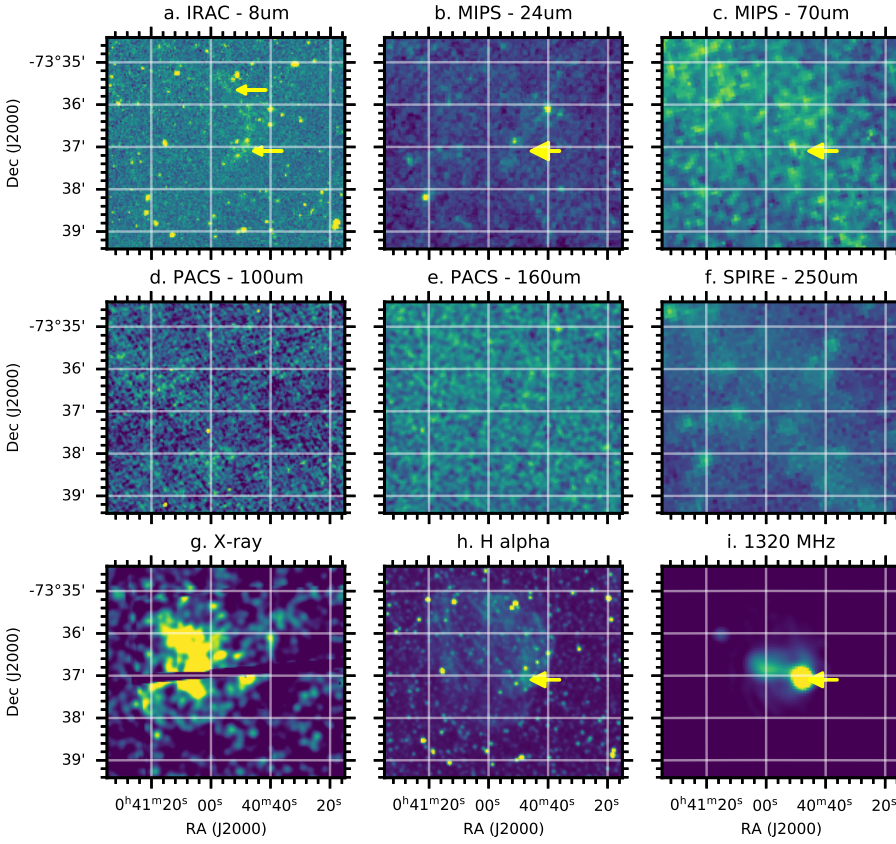


Figure 1. SNR J0040.9–7337 (B0039–73.53, DEM S5): detection. The pulsar powered bow shock is clearly seen in the 1320 MHz radio image (i), and that part of the SNR is brightest in the $H\alpha$ image. The corresponding emission is found at $8\ \mu\text{m}$. There is a discrete source detected across 8, 24, and $70\ \mu\text{m}$, as well as $H\alpha$, with a very close correlation to a strong X-ray source. Whether this is a part of the pulsar wind nebula or the pulsar itself requires further confirmation. The filaments extend from this bow shock to the north, and part of the filaments is detected at $8\ \mu\text{m}$, as if it is an arc, with a hint at $70\ \mu\text{m}$.

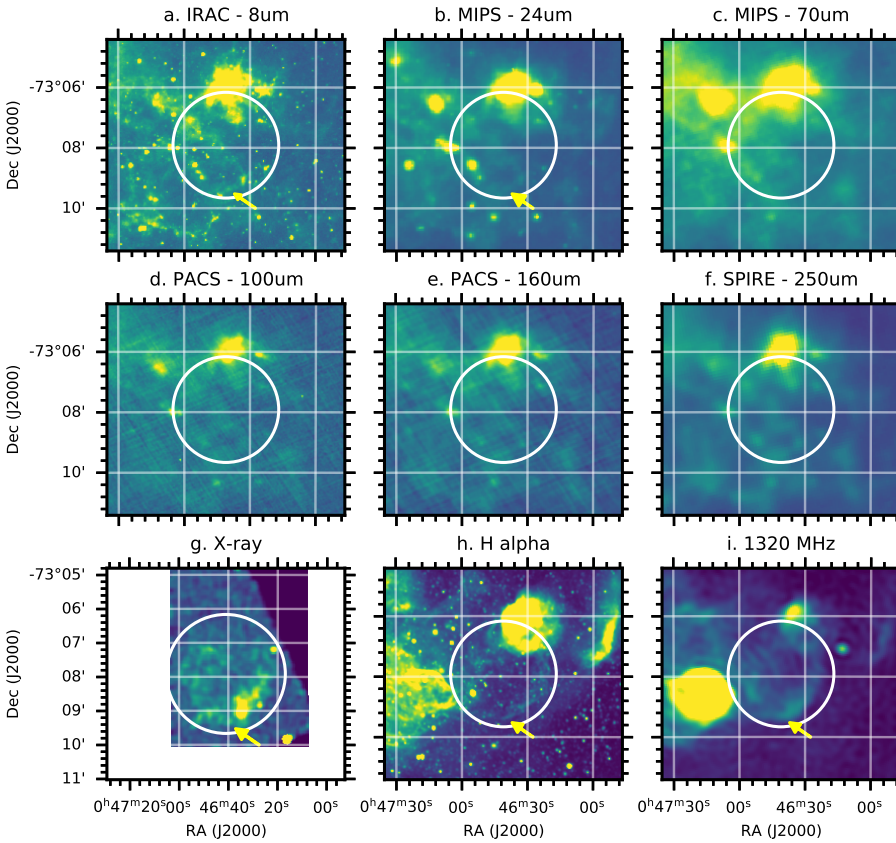


Figure 2. SNR J0046.6–7307 (B0044-73.4, DEM S32): possible detection. $H\alpha$ and 1320 MHz radio images clearly indicate shell structure, the south-west and potentially south-east part of the shell are detected in *Spitzer* 8 and $24\ \mu\text{m}$ images and possibly PACS and SPIRE 100– $250\ \mu\text{m}$. The brightest clouds found in the north of the shell are molecular clouds. The bright radio source just outside of the white circle in the south-east is SNR J0047.2–7308. A 0.3–10.0 keV band from *Chandra* is used for the X-ray image (g).

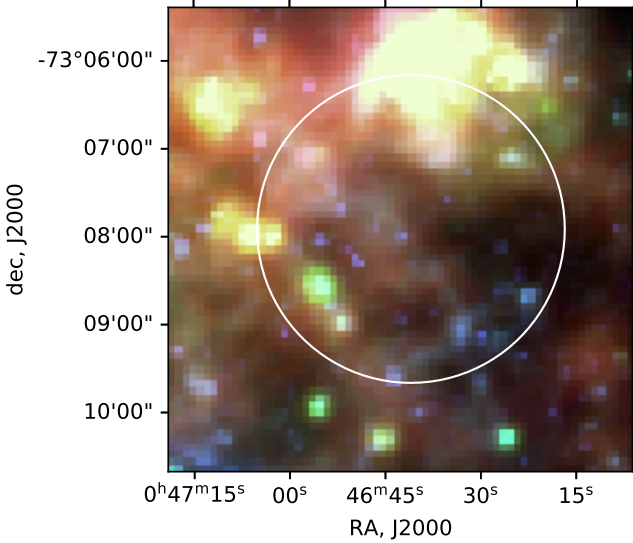


Figure 3. SNR J0046.6–7307 (B0044–73.4, DEM S32) three-colour image: $8\ \mu\text{m}$ (blue), $24\ \mu\text{m}$ (green), $70\ \mu\text{m}$ (red), indicating possible detection of the shell on south-east of the SNR, as traced by blue colour.

flow from the young stellar object (YSO) candidate S3MC J004905.49–731356.31 or possibly another YSO candidate S3MC J004914.84–731448.37 (Bolatto et al. 2007), both of which sit inside the bow shock. Alternatively, another possible source is a red supergiant candidate SSTISAGEMA J004908.72–731355.0 (Seale et al. 2014). The bow shock itself is recorded as YSO candidate S3MC J004914.84–731448.37 by Bolatto et al. (2007).

The YSO candidate, S3MC J004905.49–731356.31 (Bolatto et al. 2007) appears to be a bright red point source in Fig. 5 and is detected across all *Spitzer* and *Herschel* bands (Fig. 4). This source is located in a favourable position for causing both the bow shock and the nebulosity located to the north-east of that area (Fig. 5). High-mass YSOs can cause bow shocks associated with their jets, however, in the LMC at 50 kpc, the scale of the jets are recorded as less than 1 arcsec (McLeod et al. 2018). In contrast, the detected bow shock in the SMC is more than 60 arcsec away from the source, i.e. a much larger distance. It could be associated with a high-mass star, but it needs to be confirmed if such a large jet is possible. An alternative possibility is the red supergiant candidate SSTISAGEMA J004908.72–731355.0 (Seale et al. 2014), which is seen as a faint green point source to the east of S3MC J004905.49–731356.31 in Fig. 5. Similar to S3MC J004905.49–731356.31, its location favours it as a source of the bow shock given that mass loss from red-supergiants can trigger bow shocks, as observed in α Ori (Ueta et al. 2008; Decin et al. 2012). The bow shock in α Ori was about 7 arcmin away from the star at a distance of 197 pc (Decin et al. 2012), corresponding to only about 1.4 arcsec at SMC distance. Therefore the scale of this SMC bow shock seems to be too large to result from mass lost from a red-supergiant. The final possibility is the YSO candidate, S3MC J004914.84–731448.37, which is immediately behind the bow shock. It appears however that the star is too close to the bow shock, and the opening angle of the bow does not favour this star as a source. At this point the source of this bow shock remains unclear.

4.1.4 SNR J0052.6–7238, B0050-728, DEM S68SE: detection

SNR J0052.6–7238 the radio and $H\alpha$ images show several crescent-shaped emission features. An intersecting double crescent feature can be clearly seen in the $H\alpha$ and $24\ \mu\text{m}$ images. The two crescents in the north are indicated with an arrow in Fig. 6 b. Interestingly, in $H\alpha$ the north-west crescent is brighter than the one just south of it, whereas at $24\ \mu\text{m}$, the north-west crescent is much fainter than the one south of it. Diffuse ISM emission is detected around the crescents at 8, and $70\text{--}250\ \mu\text{m}$, but the crescent is not distinct at $8\ \mu\text{m}$.

Additionally, a multitude of crescents lay out in the south of the SNR, indicated by an arrow in the $H\alpha$ and radio images of Fig. 6. These crescents are probably detected as a diffuse cloud at $24\ \mu\text{m}$.

4.1.5 SNR J0059.4–7210, B0057-72.2, DEM S103, IKT 18: possible detection

This SNR is closely located in N66 HII region. Although it is challenging to separate SNR emission from the intervening HII region at optical wavelengths, the SNR is clearly isolated in X-ray and radio images (Ye et al. 1991; Maggi et al. 2019). Since the HII region is overwhelmingly bright in $H\alpha$ and infrared, it is not easy to separate the SNR using these wavelengths. It is possible, however, to remove thermal emission estimated from the $H\alpha$ flux from the radio-continuum images (Reid et al. 2006). The remaining non-thermal emission allows the identification of the SNR embedded in the dense N66 region.

An arc, detected inside the white circle in the $H\alpha$ image (Fig. 8), could be associated with SNR J0059.4–7210 (Danforth et al. 2003; Rubio et al. 2000). The dynamical age is estimated to be about 2×10^5 years (Danforth et al. 2003; Nota et al. 2006), using expansion velocities measured in the UV spectrum. Alternatively, this arc could potentially be a bubble formed by a mass-loss wind from Wolf-Rayet star, HD 5980 (Heydari-Malayeri & Selier 2010), which is seen as a bright point source in the $H\alpha$ image (Fig. 8 h). This arc is enlarged in Fig 9, to emphasise the emission in $24\ \mu\text{m}$ which has been assigned a green colour. It can be seen that the $24\ \mu\text{m}$ emission forms a near-circle, following inside the white circular line until it extends away to south east. Because this arc is visible, we categorise the SNR as a possible infrared detection, however, the arc could be associated with a Wolf-Rayet star rather than the SNR.

The IR image gives the impression that as the SNR expands, it is compressing the surrounding ISM gas, creating a void where only infrared emission between 24 and $100\ \mu\text{m}$ appears survive. That compression has resulted in a ‘gas deficiency’ in the north-east of N66, whereas in the western side of N66, the HII region is gradually transiting towards a PDR (photon dominated region) (Rubio et al. 2000). Detailed analysis of this region is presented in Sect 6.

4.1.6 SNR J0103.5–7247, HFPK 334: possible detection

SNR J0103.5–7247 contains a bright point source seen in X-ray and radio images, though it is largely disputed whether this source is associated with the SNR or not (Crawford et al. 2014). If the point source is associated with the SNR, it could be a compact source or pulsar wind nebula. This point source is detected at 8, 24, 70 and $250\ \mu\text{m}$ (Fig. 10), though it is very faint at 8 and $250\ \mu\text{m}$. This SNR is classified as a possible detection.

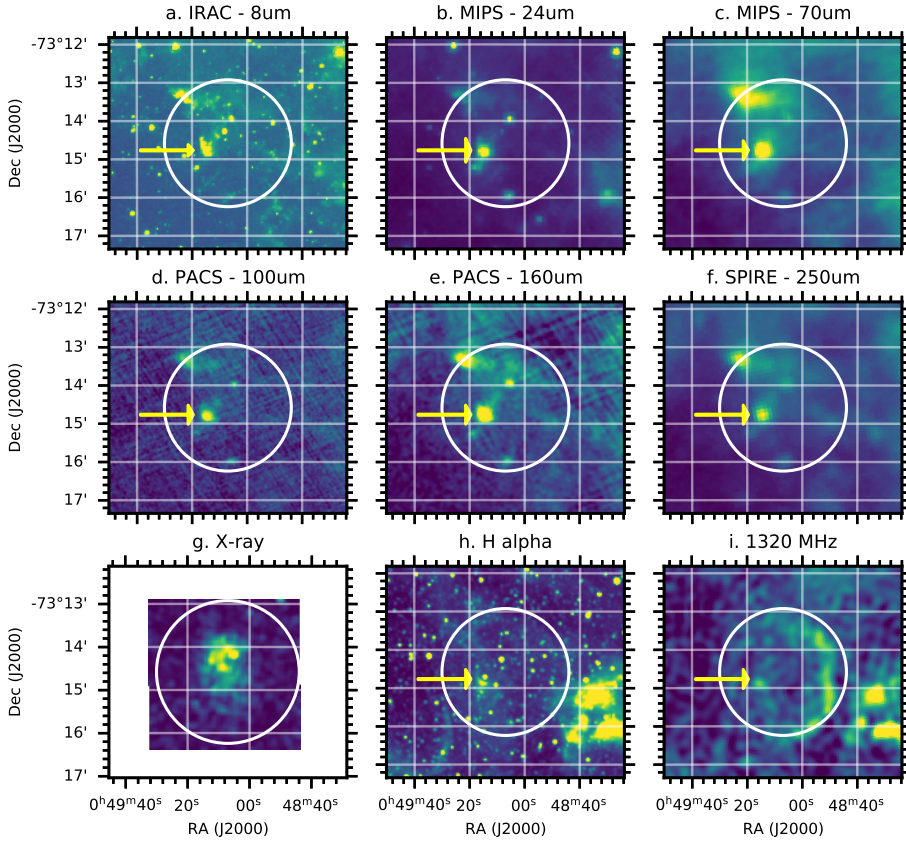


Figure 4. SNR J0049.1–7314, B0047-73.5, DEM S49, IKT 5: unlikely detection of the SNR itself, but it has a bow shock from an unknown source in the field. Panel (g) is a *Chandra* image in the 0.3–2.1 keV band.

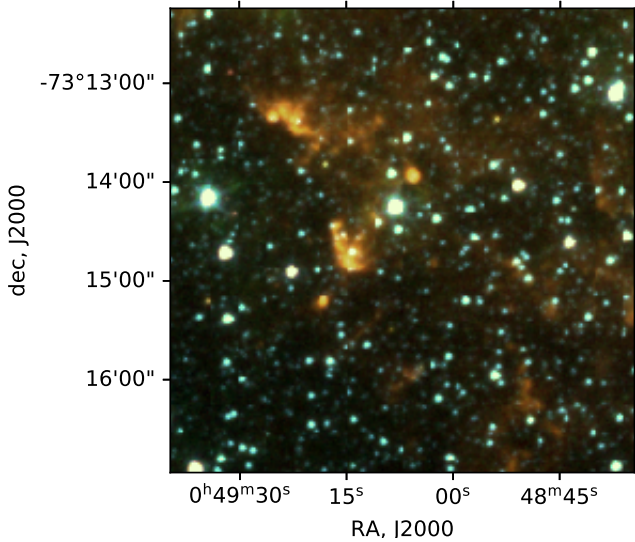


Figure 5. The 3.6 (blue), 5.8 (green) and 8.0 μm (red) three color composite image of SNR J0049.1–7314 field. Unrelated bow shock and nebulosity are detected in red colour.

4.1.7 SNR J0103.6–7201: possible detection

SNR J0103.6–7201 is a relatively new SNR reported by *XMM* (Maggi et al. 2019) and $\text{H}\alpha$ (Gvaramadze et al. 2019). There is a point source detected in the 8 μm image, and it may be a counterpart to the Be X-ray binary (Gvaramadze et al. 2019). This Be X-ray

binary has been associated with the neutron star of SXP 1323 that could have formed at the SN explosion about 40,000 years ago.

Gvaramadze et al. (2019) and Maggi et al. (2019) reported a very thin shell around SXP 1323, next to the HII region N 76, which is very bright in the $\text{H}\alpha$ image (Nazé et al. 2003a). The south-west part of this shell is pointed out with an arrow in the $\text{H}\alpha$ image in Fig.11. In the infrared, the emission is dominated by unrelated ISM emission, with some contribution from N 76 at IRAC 8 μm and 24 μm . No evidence of an SNR shell is found in the infrared.

4.1.8 SNR J0104.0–7202, B0102-72.3, DEM S124, IKT 22: detection

SNR J0104.0–7202, or commonly known as 1E 0102.2–7291, is one of the best studied SNRs in the SMC. Its dust emission was detected by *Spitzer* (Stanimirović et al. 2005), initially as a part of the SMC survey (Bolatto et al. 2007), later followed by dedicated spectral mapping observations using *Spitzer* IRS (Sandstrom et al. 2009; Rho et al. 2009). From X-ray spectra, it is known to be oxygen-rich, suggesting that this SNR is a high-mass, core-collapse SN in origin (Dopita et al. 1981). A candidate of the compact object has been reported by Vogt et al. (2018), though it has not been established whether this is really a compact object or not (Hebbar et al. 2020; Long et al. 2020). The estimated age of this SNR is from ~ 1000 up to 3500 yrs (Tuohy et al. 1983; Alan et al. 2019), and the progenitor is potentially of high-mass stellar origin ($40 M_{\odot}$; Alan et al. 2019). The infrared emission is associated with the X-ray and radio ejecta with the brightest positions or clumps in 24 μm closely resembling the brightest positions in [O III]. The estimated ejecta

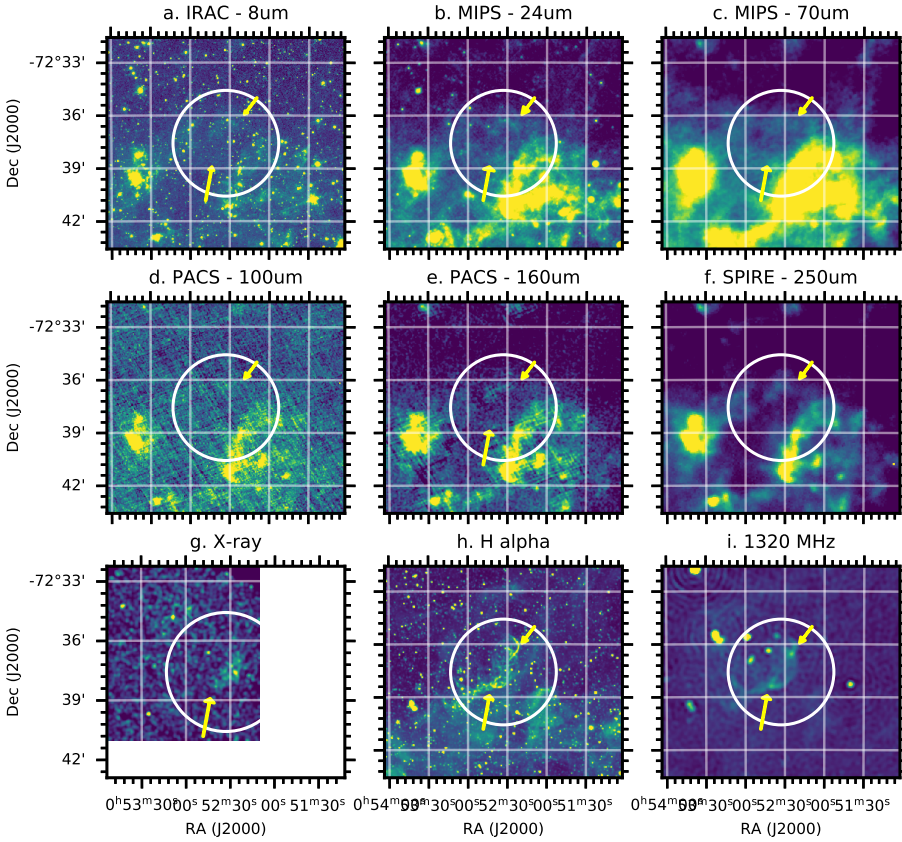


Figure 6. SNR J0052.6–7238, B0050-728, DEM S68SE: detection. Part of shells or filaments have been detected in the north, and potentially in the south at $8\ \mu\text{m}$, $24\ \mu\text{m}$ and $70\ \mu\text{m}$. Panel (g) is a *Chandra* image in the 0.3–2.1 keV band.

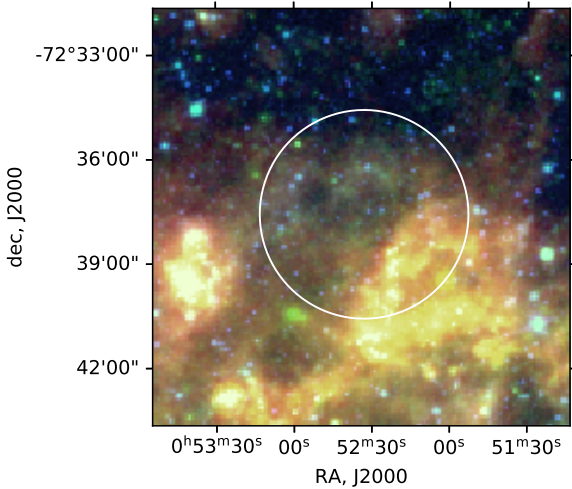


Figure 7. SNR J0052.6–7238, B0050-728, DEM S68SE. The 8 (blue), 24 (green) and $70\ \mu\text{m}$ (red) three colour composite image - probably detected.

dust mass from *Spitzer* IRS is about $3 \times 10^{-3} M_{\odot}$ (Sandstrom et al. 2009) to $0.01 M_{\odot}$ (Rho et al. 2009).

As reported by Stanimirović et al. (2005) and Sandstrom et al. (2009), the SNR is clearly visible at $24\ \mu\text{m}$. Herschel SNR dedicated observations (Proposal ID: 2011hers.prop.1802S) took images at 70 and $100\ \mu\text{m}$, resulting in a clear detection at these wavelengths

(Fig. 12). At $8\ \mu\text{m}$, two very faint points are detected, the southerly one corresponds to $24\ \mu\text{m}$ bright clump, and the other in the east has a counterpart with an X-ray clump. This SNR is located very close to the HII region LHA 115-N76C, which can be seen southwest of SNR J0104.0–7202 (Fig. 12). This HII region is brighter than the SNR at infrared wavelengths. At $8\ \mu\text{m}$, the SNR is faint but probably buried within unrelated ISM clouds, presumably with polycyclic aromatic hydrocarbons (PAHs) from the HII region and surroundings. The cold dust emission from this HII region and surroundings dominates at $250\ \mu\text{m}$, and contributes some emission at $160\ \mu\text{m}$. In Fig. 12, panel h shows [O III] image, instead of $H\alpha$, as this O-rich SNR stands out better at [O III] than $H\alpha$.

4.1.9 SNR J0105.6–7204, DEM S128: possible detection

There is a confusion of source names and coordinates for SNR J0105.6–7204 and SNR J0105.6–7209. Davies et al. (1976) listed SNR J0105.6–7204 (DEM S128) and SNR J0105.6–7209 (DEM S130) in their $H\alpha$ + [N II] photographic plates, however, the coordinates in the table and the location on the photographic plates have been mixed up: coordinates read from photographic plates for DEM S128 correspond to the coordinates for DEM S130 listed in their Table 4. Filipovic et al. (2005) and Filipovic et al. (2008) listed J010524–720923 as a SNR DEM S128, and J010539–720341 as a SNR candidate DEM S 130. Maggi et al. (2019) concluded J010539–720341 is probably not an SNR. Therefore, we investigate only SNR J0105.6–7204 as the SNR DEM S128. The coordinates and the size of this SNR are taken from *XMM* analysis (Haberl et al. 2012).

In the optical and radio, the north shell extends beyond the

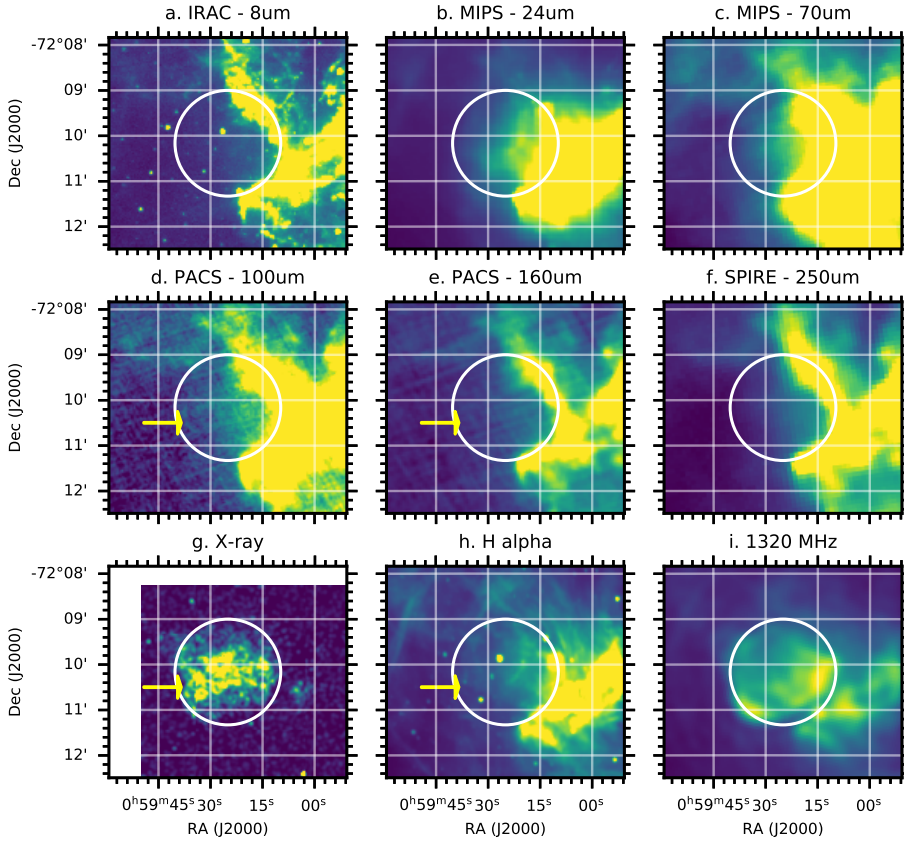


Figure 8. SNR J0059.4–7210, B0057-72.2, DEM S103, IKT 18: possible detection. Panel (g) is a *Chandra* image in the 0.3–2.1 keV band.

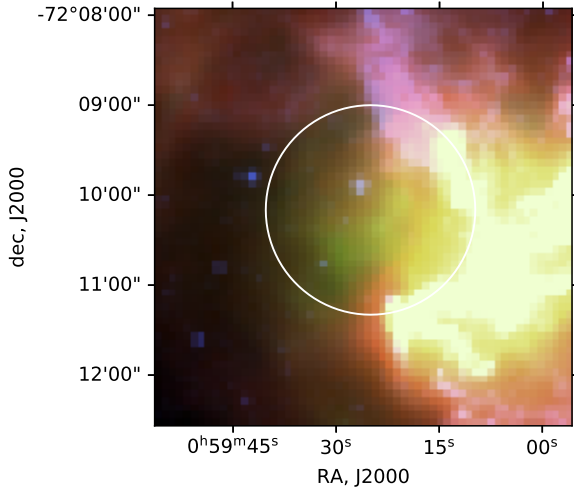


Figure 9. SNR J0059.4–7210, B0057-72.2, DEM S103, IKT 18. The $8\ \mu\text{m}$ (blue), $24\ \mu\text{m}$ (green) and $70\ \mu\text{m}$ (red) three colour composite image with a possible detection of filaments, seen as green near-circular’ filaments within the white circle.

X-ray shell (Fig. 13), as pointed out by Maggi et al. (2019). That shell is also noticeable in infrared images, at least at $8\ \mu\text{m}$ and $24\ \mu\text{m}$, and potentially at $160\ \mu\text{m}$ and $250\ \mu\text{m}$ (Fig. 13). This SNR has been suggested to be type Ia origin (Roper et al. 2015). As it is bright at $250\ \mu\text{m}$, the north shell might be tracing the place where the SNR

interacts the most with nearby ISM, as found in Galactic type Ia, Tycho (Gomez et al. 2012a)

4.1.10 SNR J0106.2–7205, B0104-72.3, IKT 25: detection

There is a debate as to whether SNR J0106.2–7205 is of core-collapse or type Ia SN origin. Lee et al. (2011) and Roper et al. (2015) suggested it is a type Ia candidate, due to the high Fe abundance based on *XMM* and *Chandra* spectra. Lopez et al. (2014) and Maggi et al. (2019) found that the previous abundance analysis contains an error, and suggests core-collapse origin. If it is a core-collapse SNR, the estimated age is 18,000 yrs old, with a progenitor mass of $18 M_{\odot}$ (Katsuda et al. 2018)

Lee et al. (2011) reported a detection using both IRAC $8\ \mu\text{m}$ and *AKARI* (Koo et al. 2007). We detect this SNR across *Spitzer* and *Herschel* images, though it is very faint at $100\ \mu\text{m}$ (Fig. 14). There is a difference in morphology between X-ray and $\text{H}\alpha$ +radio+IR, with the shapes and locations of IR resembling those of $\text{H}\alpha$ more closely.

4.1.11 SNR J0127.7–7332, SXP 1062: detection

SNR J0127.7–7332 shows shell-type structure, with the brightest rim at the south in the radio, while the northern shell is brighter in the optical image (Fig. 15; Maggi et al. 2019). The central source is associated with a Be/X-ray binary, containing a pulsar SXP 1062 (Maggi et al. 2019) and is detected here at $8\ \mu\text{m}$. Additionally, a small blob, which might be a part of north shell, is detected across infrared images (Fig. 15).

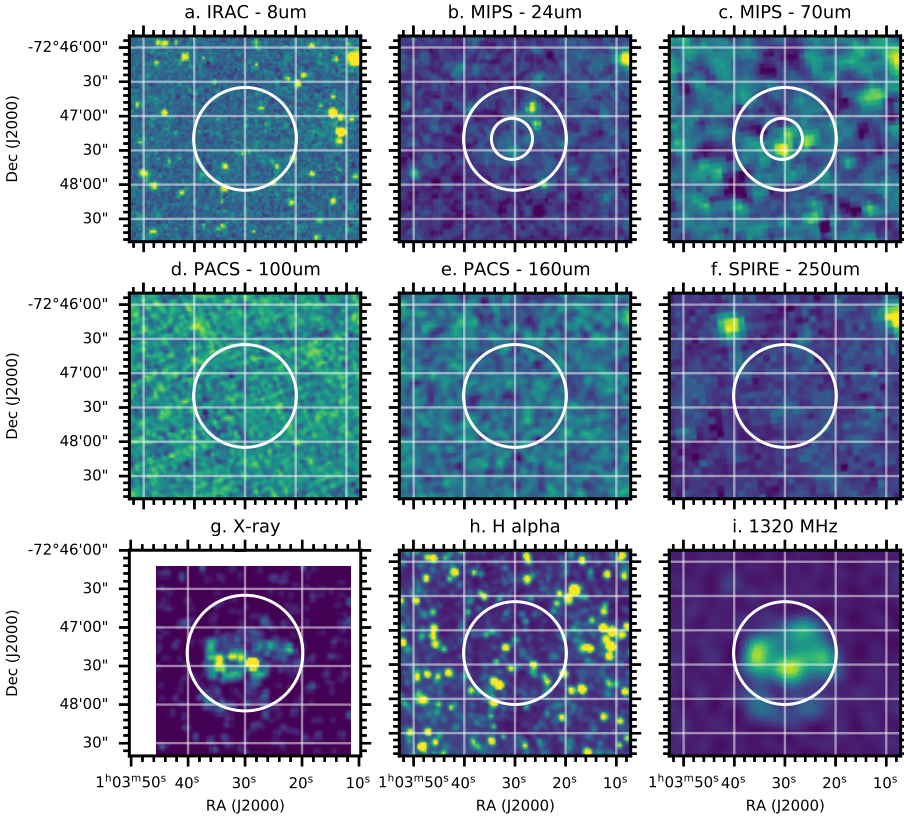


Figure 10. SNR J0103.5–7247, HFPK 334: possible detection. Panel (g) shows a *Chandra* image in the 0.44–1.17 keV band

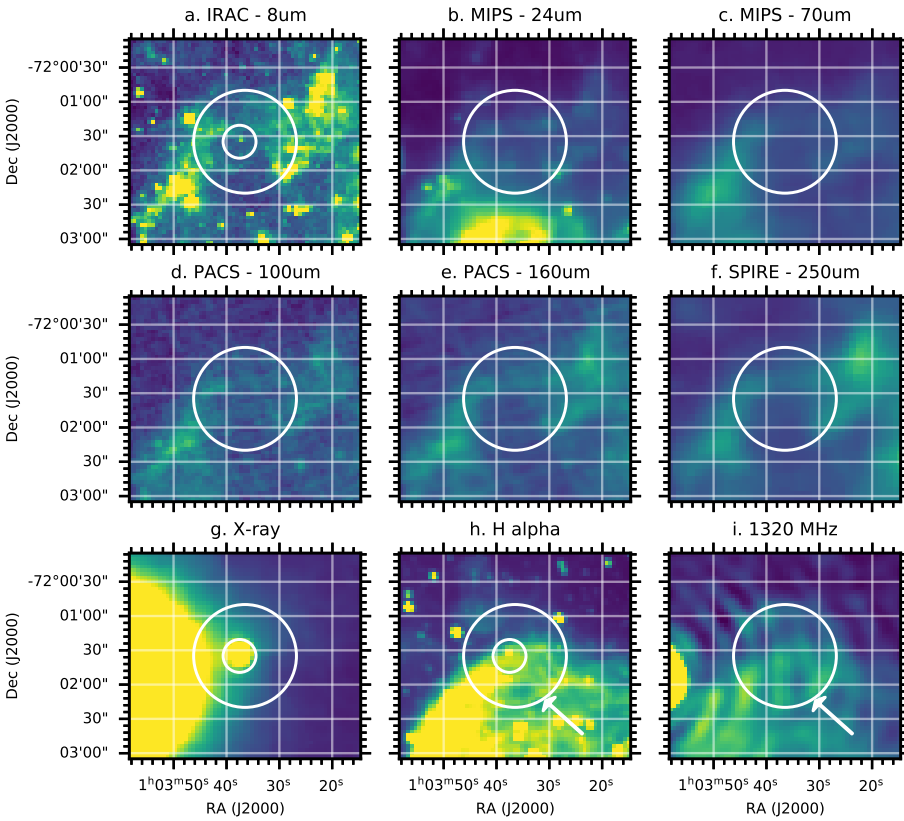


Figure 11. SNR J0103.6–7201: possible detection of a point source, which may be a neutron star associated with this SNR. Note that arcs in the radio image (i) are an airy disc from the bright source to the east of the SNR.

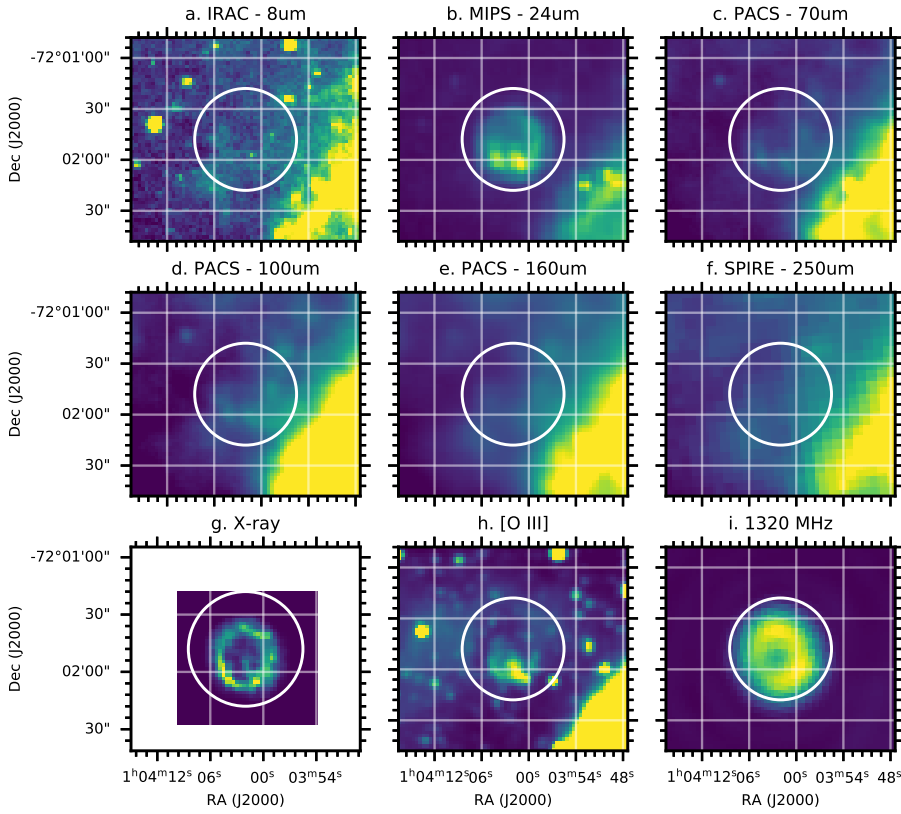


Figure 12. SNR J0104.0–7202, B0102-72.3, DEM S124, IKT 22, or commonly known as 1E 0102.2–7291: detection. Panel (g) is a *Chandra* image in the 0.3–10.0 keV band, and panel (h) is an [O III] image, as this oxygen-rich SNR stands more at [O III] than at $H\alpha$.

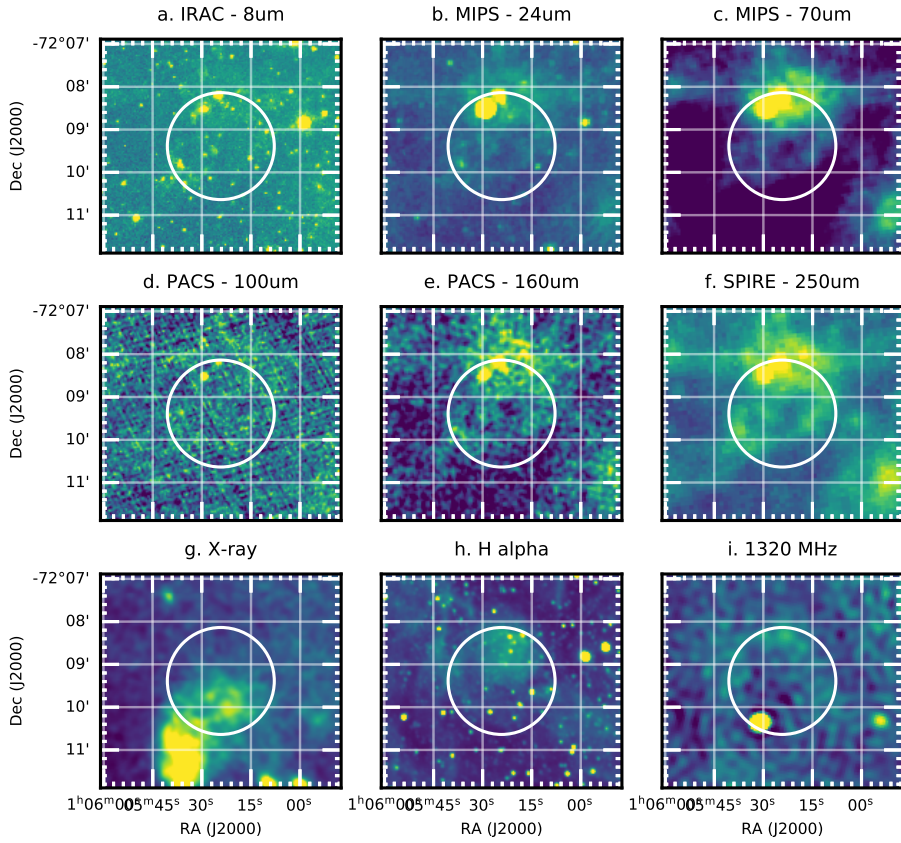


Figure 13. SNR J0105.6–7209, B0104-72.2, DEM S130: possible detection

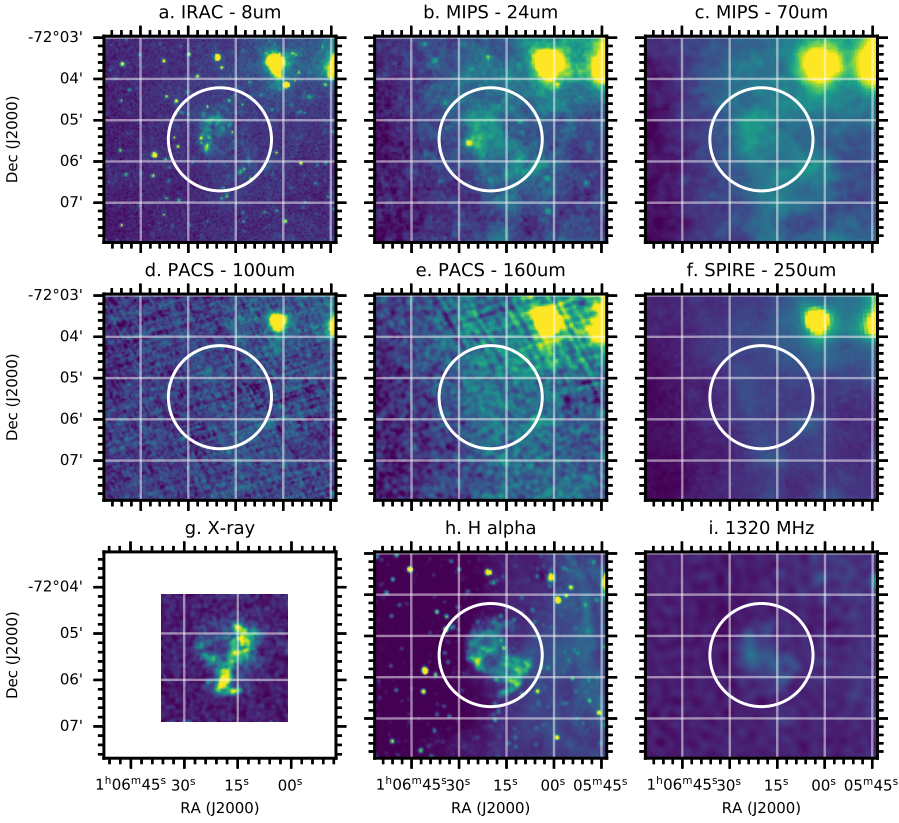


Figure 14. SNR J0106.2–7205, B0104-72.3, IKT 25: detection. Panel (g) is a *Chandra* image in the 0.3–10.0 keV band

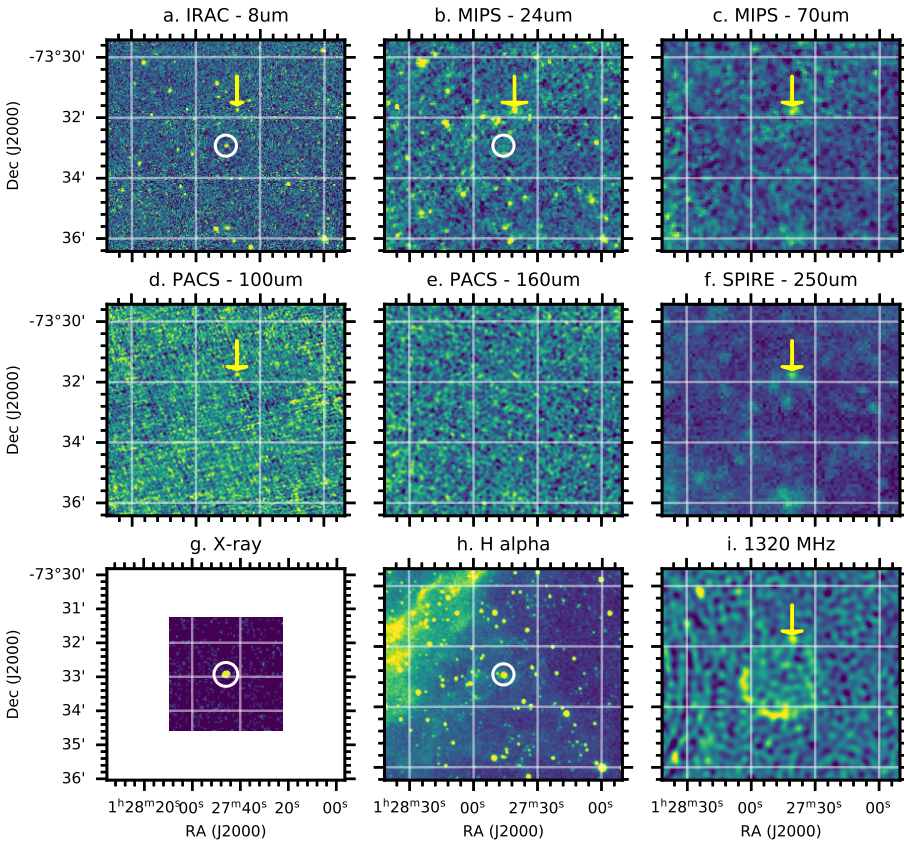


Figure 15. SNR J0127.7–7332 : detection of the pulsar SXP 1062, is indicated by a circle. There is an additional detection of small ‘blob’ in the north possibly associated with the shell. Panel (g) is a *Chandra* image in the 0.3–10.0 keV band

5 ANALYSIS OF DUST EMISSION

From the 24 SMC SNRs, we make a positive section from only 5. Two detections are associated with pulsars or pulsar wind nebulae, and only 3 detections are associated with expanding forward-shocked regions of the SNRs. Another 5 have possible detections. The remaining 14 SNRs turned out to be non-detections both in *Spitzer* and *Herschel* bands. The number of the detections of forward-shocked regions in the infrared is relatively small. In order to understand this low detection rate, we make a simple calculation of the expected brightness of dust emission from SNRs under forward shocks, and compare it with the measured brightness.

5.1 Predicted emission from collisionally heated dust grains

As a SNR expands, the gas plunges into the ISM, sweeping up the ambient ISM gas and dust and causing a shock at the expanding boundary. In shocked regions, dust grains are heated up by the collision of fast moving electrons, and destroyed by the collision of high velocity ions and atoms, as well as dust grains (Jones et al. 1994). These forward shocks are considered to be one of the main dust destruction processes in the ISM, and determine the lifetime of the ISM dust grains (e.g. Jones et al. 1996; Micelotta et al. 2018). There are several processes involved in dust destruction. Fast moving particles sputter atoms from the surface of the dust grains, and in high velocity shocks, this sputtering process is very efficient (Dwek & Arendt 1992). Grain-grain collisions can destroy dust grains at much lower speeds, though more recent simulations demonstrate that coupling sputtering and grain-grain collisions may cause much more damage than a simply adding these two processes (Kirchschlager et al. 2019).

In shocked regions, fast moving electrons play a role in heating dust via collisions. Dwek & Arendt (1992) described the collisional heating rate of dust grains, $H(a)$ as

$$H(a) = 2\pi a^2 n_e \left(\frac{8kT_e}{\pi m_e} \right)^{1/2} kT_e \xi \quad (1)$$

where T_e is the electron temperature, m_e is electron mass, n_e is the electron density, and a is the grain size. The equation is based on a combination of the cross section of a grain, average Boltzmann velocity, and the kinetic energy of an electron. Whether an electron goes through a dust grain or not depends on the grain size and the electron temperature, which ξ represents. Dwek & Smith (1996) and Dwek et al. (2008) demonstrated that at a grain size of 0.01 and 0.1 μm , the majority of electrons can be stopped, i.e. $\xi=1$. If grain size is smaller than that range, it is likely to get slightly smaller than 1, however, it has only minor impact, and at a moment, for simplicity, we adopt $\xi=1$ across. This heating rate is in equilibrium with the radiation from dust grains ($L_\lambda = 4\pi a^2 B_\lambda Q_\lambda$), where Q_λ is the dust emissivity at wavelength λ . For simplicity, Q_λ is replaced with the Planck averaged dust emissivity

$$\langle Q(T, a) \rangle = \frac{\int B_\lambda(T) Q_{\text{abs},\lambda} d\lambda}{\int B_\lambda(T) d\lambda} \quad (2)$$

Although Dwek & Arendt (1992) adopted

$$\langle Q(T) \rangle / a \propto T_d^2 \quad (3)$$

following Draine & Lee (1984) and Draine (2011), this is a valid approximation up to ~ 60 K. Unfortunately, small grains may exceed this temperature range, so we therefore calculated $\langle Q(T_d, a) \rangle$, using the Q_λ for silicates (Ossenkopf et al. 1992). The equilibrium temperature of the dust grains is then obtained by assimilating $H(a)$,

whereby the total luminosity becomes (Chawner 2020)

$$L(a) = 4\pi a^2 \sigma T_d^4 \langle Q(a, T_d) \rangle. \quad (4)$$

We calculate the spectrum of the dust emission, using the grey body, i.e., $L_\lambda = 4\pi a^2 B_\lambda(T_d) Q_\lambda$, and Q_λ as calculated for silicates (Ossenkopf et al. 1992). We tested a mixture of silicates and amorphous carbon (Zubko et al. 1996), adopting dust-to-gas mass ratios of the Milky Way for silicates (9×10^{-3}) and amorphous carbon (1.4×10^{-3}) (Tielens 2010), and the fact that elemental abundance ratios for the Milky Way and Magellanic Clouds are similar (Gordon et al. 2014). However, the mid-infrared emission is dominated by silicate emission, and for simplicity, we only used silicates for the rest of our discussions.

The total emission from all grains is calculated by integrating L_λ across grain sizes a . We start with the smallest grain size (a_{min}) of 0.005 μm and the largest grain size (a_{max}) is 0.25 μm , following the SMC ISM value (Weingartner & Draine 2001). The smallest grain size is much smaller than the value of 0.023 μm adopted by Dwek et al. (2008) for SN 1987A's circumstellar ring, but the largest grain size is the same as that given by Dwek et al. (2008). The power law index of -3.5 is used for the number distribution of dust grains (Mathis et al. 1977).

We estimated the electron density n_e and electron temperature T_e from X-ray observations of SNRs. Maggi et al. (2019) listed T_e and emission measure EM of SMC SNRs, and n_e is estimated from $n_e = 1/f\sqrt{EM/V}$, where f is the filling factor, and V is the volume of the SNR. The filling factor is assumed to be 1 (Maggi et al. 2019), initially, and V is calculated from the diameters in Table 1. Maggi et al. (2019) also used EM to estimate hydrogen density n_H as $n_H = 1/f\sqrt{EM}/1.2V$, where a factor of 1.2 represents the difference between hydrogen and electron numbers for a fully ionised gas. The diameters in this table have been measured in radio even though radio and X-ray diameters might be different. Maggi et al. (2019) showed that the majority of SMC SNRs have a hydrogen density n_H of about 0.03–0.06 cm^{-3} (Table 2).

Finally, we estimate the dust mass swept up by SNRs, assuming all swept up dust grains survive the shocks. That is calculated from the volume V of the SNR, ISM hydrogen density n_H or $n_{H,\text{ISM}}$ and the gas-to-dust mass ratio in the ISM. Temim et al. (2015) estimated the local ISM hydrogen density, using the HI emission line, and estimated the line of sight depth of the SMC, the values of which we used for $n_{H,\text{ISM}}$. All SMC SNRs have an $n_{H,\text{ISM}}$ range of 0.5–1.9 cm^{-3} . As found in Table 2, the values of $n_{H,\text{ISM}}$ are about 10–20 times higher than those of n_H , estimated from SNR EM by Maggi et al. (2019). Subsequently, this also affects the estimated swept up dust mass by the same factor. We will discuss this discrepancy later in Sect. 5.2. Finally the gas-to-dust mass is assumed to be 500 (Gordon et al. 2014). This is the smallest value within the range (500–1300), expected from the elemental abundance (Gordon et al. 2014).

5.2 Dust emission from a SNR

We take SNR J0106.2–7205 (ITK 25) as an example of the predicted emission from dust grains, swept-up by an SNR.

Case 1 (blue line) in Figure 16 shows the predicted dust emission from SNR J0106.2–7205 (ITK 25), assuming that all swept up dust can survive SNR-ISM shocks. The swept-up dust mass is estimated, using the hydrogen density n_H from the X-ray emission measure (Maggi et al. 2019). Case 2 (red line) shows the predicted dust emission, using the hydrogen density $n_{H,\text{ISM}}$ from the HI emission line (Temim et al. 2015). Fig. 16 includes approximate average

brightnesses of SNR J0106.2–7205 at MIPS 24 and MIPS 70 μm bands, indicated by circles. The large uncertainties in the surface brightnesses are caused by uncertainties in estimating ‘background’ levels, as they are inconsistent across the span of the SNR. The total surface brightness of the background and SNR in MIPS 24 μm is above the sensitivity limit however MIPS 24 brightness range goes below the sensitivity limit (5σ) after ‘background’ subtraction. The predicted emission of case 1 is much closer to the approximate surface brightness of SNR J0106.2–7205 (ITK 25). This one assumes that all swept-up dust grains survive shocks, i.e. no dust destruction. However, there is a caveat to this interpretation.

As mentioned in Sect. 5.1, there is a factor of 10–20 discrepancy in two different methods of estimating hydrogen densities. The one from X-ray EM is $n_{\text{H}}=0.04\text{ cm}^{-3}$, while HI along the line of sight gives $n_{\text{H,ISM}}=0.9\text{ cm}^{-3}$. The obvious cause of this difference is the assumed size of the SNR, hence, its volume used for converting EM to n_{H} . As seen in Fig. 14, this SNR has an irregular shape, and the size we applied is the largest radius, assuming symmetric shape, so that reducing the radius is reasonable. Increasing the radius by a factor 2 can increase n_{H} to 0.3 cm^{-3} . Naturally, by reducing the estimated radius, and hence the volume, the total dust mass also reduces. On the other hand, by reducing the volume, the electron density, n_e goes up by a factor of \sqrt{V} , increasing the total heating. Therefore, reducing the size by a factor of 2 causes the emission to look like case 3 in Fig. 16, where dust is warmer than case 1 and overall emission is increased. The temperature of the smallest grain is 60 K for case 1, and 71 K for case 3. In this case, the 24 μm surface brightness is over-predicted by a factor of 5–10.

We can make a further experiment by matching the n_{H} and $n_{\text{H,ISM}}$ by decreasing the filling factor f from 1 to 0.1 for n_{H} , as $n_{\text{H}} = 1/f\sqrt{EM/1.2V}$. The radius is kept at the initial size. In this case, n_e goes up by a factor of 10, i.e. an increase in the heating source, and the total dust mass increases by a factor of 10 over and above case 1 (but the dust mass remains the same as case 2), resulting in a much hotter and brighter dust emission (case 4 in Fig. 16). The smallest grain has an equilibrium temperature of 86 K in case 4, much hotter than 60 K for case 1. Case 4 is very unlikely, because it over-predicts 24 μm flux by a factor of 200–400.

One possible way to accept the low filling factor described in case 4, but to match the observed brightness would be to remove the small dust grains from the equation. Because smaller grains tend to reach higher equilibrium temperature, removing small grains can result in reducing emission at shorter wavelengths, thereby also reducing overall emission. Case 5 demonstrates dust emission only limited from grains between 0.18–0.25 μm , instead of default 0.005–0.25 μm as in case 4. The total dust mass is reduced to only 18% of case 4, i.e. equivalent to a scenario where smaller dust grains have been destroyed by SN shocks, and only larger dust grains survived. Since large grains tend to have lower dust temperatures than small grains, the model can reproduce the measured surface brightness reasonably well.

Note that very small grains might not reach equilibrium temperature, but instead they can reach higher temperatures. Once small grains absorb the energy from photons, their temperature spikes up, instantly. However, this makes the overall emission much hotter and much brighter, so that the discrepancies between the measured brightness and predicted brightness in case 2 or 3 would worsen.

There is about 10% numerical error in the model brightness, so that the difference between n_{H} and $n_{\text{H,ISM}}$ does not linearly reflected in F_{24}/F'_{24} or F_{70}/F'_{70} in Table 2.

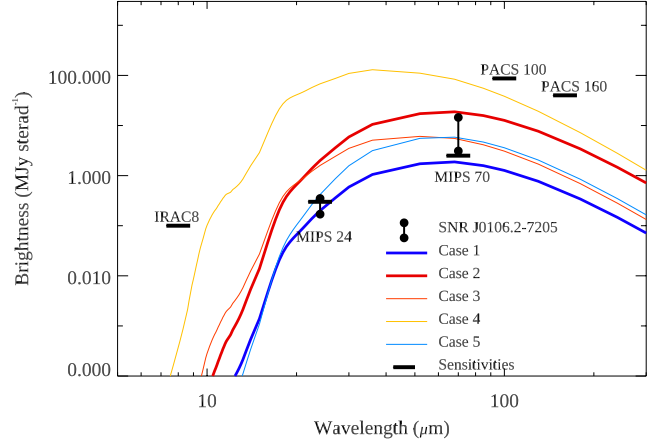


Figure 16. The expected dust emission from an SNR, an example using SNR J0106.2–7205 (ITK 25), comparing approximate brightness at MIPS 24 and 70 μm fluxes (black circles). Case 1 and case 2 show expected dust emission, using n_{H} and $n_{\text{H,ISM}}$, respectively, assuming that all ISM swept up dust fills a disk within the SNR radius. Case 3 demonstrates the emission, if the radius of the SNR is half of the one used for cases 1 and 2. Case 4 using the filling factor of 0.1, instead of 1 for the SNR, increasing the value of n_{H} to match $n_{\text{H,ISM}}$. That would also increase n_e , hence, more heating source. Case 5 (blue thick line) shows the case when only large dust grains (0.18–0.25 μm) are included. Case 5 approximates closely to the MIPS 24 and 70 μm brightness (black circles).

6 DUST TEMPERATURE AND DENSITY ANALYSIS OF SNR J0059.4–7210 (DSMS103)

As the SNR J0059.4–7210 (DSMS103) looks as if it collides with the star-forming region NGC 346, we investigate its effect on dust, using *Spitzer* and *Herschel* images.

6.1 Analysis

We used *Spitzer* MIPS 24 and 70 μm , *Herschel* PACS 100 and 160 μm and SPIRE 250 μm images.

Only for this analysis, we used residual images from SAGE-SMC for MIPS 24 and 70 μm bands. The residual images are the images after point sources were subtracted. These removed point sources include bright clusters in the star-forming regions of NGC 346. All images were smoothed to have a 6 arcsec pixel pitch, matching to the coarsest angular resolution of the *Herschel* SPIRE 250 μm band. *Spitzer* and *Herschel* uncertainty maps were used as a σ for fitting a grey body. As found in the images, the PACS 100 μm image has much larger uncertainties, due to its lower spatial sampling rate. The *Herschel* uncertainty maps reflect this issue, and the weight of 100 μm intensities is much lower than the rest of the *Spitzer* and *Herschel* images. We also removed S/N < 10 regions in the final fitted results.

The *Spitzer* and *Herschel* images were fitted pixel to pixel, using the grey body of the dust emission. The surface brightness of the dust S_{ν} is associated with the temperature as $S_{\nu} = \kappa_{\nu}\Sigma_d B_{\nu}(T_d)$, where $B_{\nu}(T_d)$ is the Planck function. We used an equation from Gordon et al. (2014), $S_{\nu} = (2.0891 \times 10^{-4})\kappa_{\nu}\Sigma_d B_{\nu}(T_d)$, where the dust surface mass density Σ_d is in $M_{\odot}\text{pc}^{-2}$, the dust emissivity κ_{ν} in $\text{cm}^2\text{ g}^{-1}$ and S_{ν} and $B_{\nu}(T_d)$ in MJy sr^{-1} . The κ_{ν} , was calculated by dust emissivity law $\kappa_{\lambda}=\kappa_{\lambda_0}(\lambda/\lambda_0)^{-\beta}$ from Hildebrand (1983). We adopted the power law index of $\beta = 1.9$ from Planck Galactic plane studies (Collaboration et al. 2014), which is consistent with

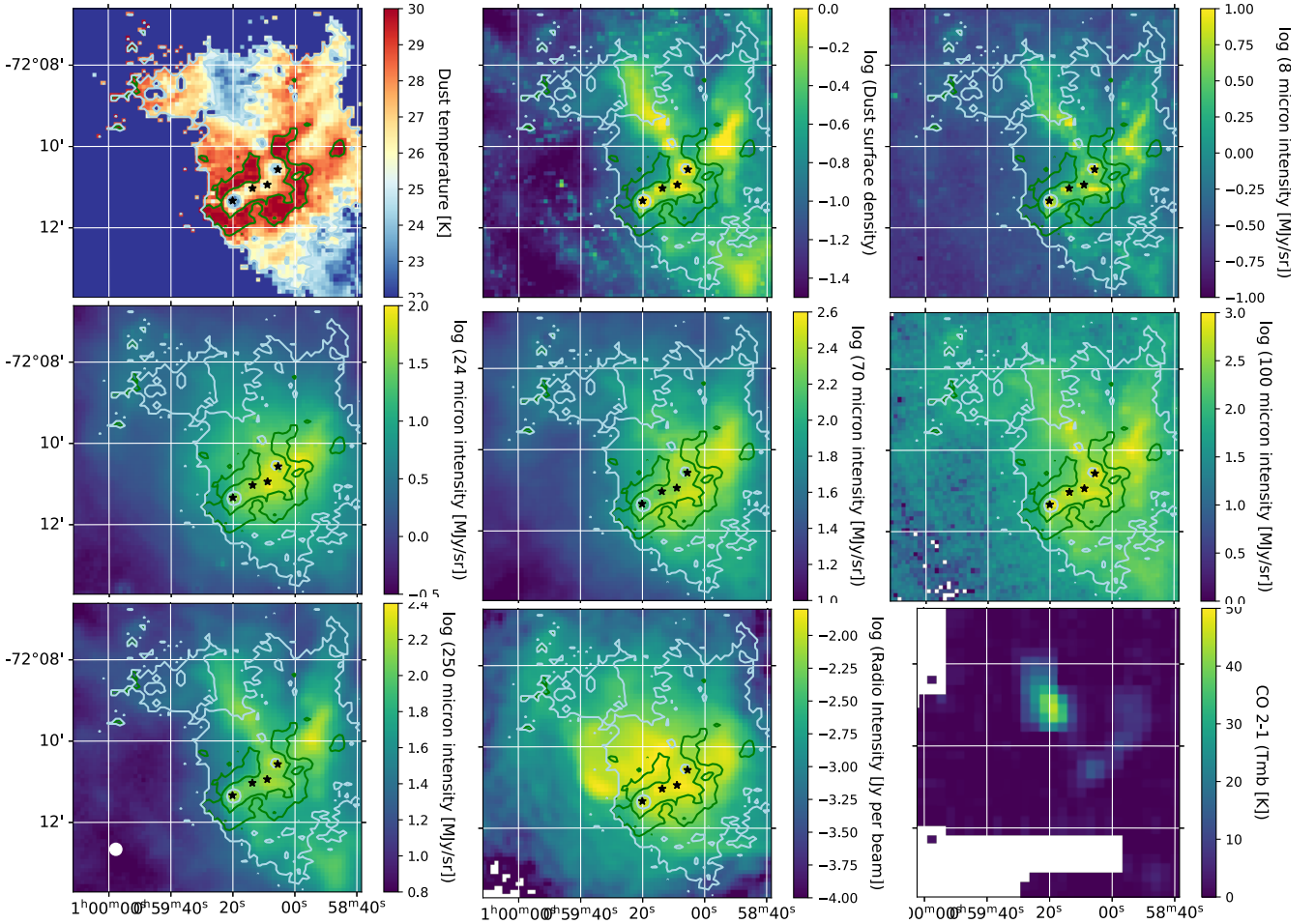


Figure 17. Dust temperature T_d , and surface density Σ_d maps, together with *Spitzer*, *Herschel*, radio and CO 2–1 maps of SNR J0059.4–7210 (DSM S103). The line contours trace the dust temperature of 29 K (green) and 15 K (light blue). The white circle in 250 μm map shows the SPIRE 250 μm beam size. *Spitzer* and *Herschel* images are smoothed to the SPIRE 250 μm angular resolution. Black star marks show the locations of clusters which exhibit colder dust temperatures.

the estimated β at SNR-ISM interacting regions in the Galactic plane (Chawner et al. 2019). Grain density ρ of $0.27 \text{ m}^2 \text{ kg}^{-1}$ at 450 μm is adopted from Gomez et al. (2010). These properties are overall consistent with the estimated the ranges of dust properties, reported in the SMC ISM (Gordon et al. 2014).

CO $J=2-1$ observations of SNR DEM S103 were obtained, using the Atacama Pathfinder Experiment (APEX) with Heterodyne SIS detector, nFLASH. The data were acquired intermittently from 9th to 14th of December 2020, in OTF mapping mode, and its T_{mb} map is plotted in right bottom panel of Fig. 17.

6.2 Results

Fig. 17 shows the resultant dust temperature T_d and the dust surface mass density Σ_d in SNR DEM S103 and the neighbouring star-forming region NGC 346. The top panel shows T_d (left) and Σ_d (right). The contour of T_d is overlaid in *Spitzer* 8, 24, *Herschel* 70, 100, 250 and radio images in the top right, the middle, the bottom left and central panels.

In the south-east region of, NGC 346, the T_d is lower (~ 22 K) at the locations of stellar clusters, marked by stars in Fig. 17. These stellar clusters are surrounded by higher (about 30 K) dust tempera-

ture regions. We carefully examined these low temperature regions in the *Spitzer* and *Herschel* images as they contain stellar clusters which could have potentially been removed as point sources in the *Spitzer* residual images, thereby artificially lowering the inferred dust temperature. However, the low temperature is mainly determined through the *Herschel* images, and these images show little contribution from the stars, hence, we can be confident that the cold dust at these stellar cluster locations is real. Surprisingly, these low T_d regions have bright radio emission. In contrast, the surrounding higher T_d region has fainter radio emission. Between DEM S103 and NGC 346, there is a higher T_d region, and this region corresponds to the gap in radio emission between DEM S103 and NGC 346.

The stellar cluster regions, marked with stars in Fig. 17, have colder T_d , with the highest Σ_d . Although the dust mass has T_d dependence, because the fitting procedure involves $B_\nu(T_d)$, the difference in dust mass is much larger than what can be explained by $B_\nu(T_d)$ at 22 K and 30 K: the difference is 0.49 and 0.33 dex at 160 and 250 μm , so that bright infrared emission from these cluster regions is explained by more dust mass towards these regions. There is negligible contribution ($< 0.1\%$) of synchrotron radiation at 24–250 μm wavelengths, estimated from radio 960 MHz and 1320 MHz

images (Joseph et al. 2019). Very low levels of synchrotron and free-free agree with the analysis of SMC molecular clouds by Takekoshi et al. (2017). Further, the $250\ \mu\text{m}$ emission, which picks up colder dust, is brighter within this region. Hence, indeed, this area has a higher dust mass, as confirmed in the dust mass map. Some of the dust emission corresponds to filaments being extinguished against the HII region, seen by the optical *HST* image (Nota et al. 2006). Although not clearly detected in our nFLASH CO image, CO emission was detected in this region in previous mapping (Rubio et al. 2000; Hony et al. 2015).

In the north-west of NGC 346, the dust temperature is low ($\sim 22\text{--}23\ \text{K}$). The low temperature region is not localised at the stellar clusters only, but throughout the entire region, covering multiple stellar clusters and their surrounding regions. That is in contrast to the southern part of NGC 346, where the low dust temperature is localised at stellar clusters only. Also in the north-western region, there is little radio continuum emission detected, but CO is brightest.

On the west, outside of the green contour line, infrared emission is bright, but it is caused by combination of both moderately high temperature (26 K) and high dust mass.

Note that if the S/N is below 10 at $100\ \mu\text{m}$ intensity, the temperature has been masked. In the figure, this masked region was assigned a 20 K colour, but this is not a true reflection of the actual temperature. Low temperature regions tend to have less far-infrared emission, hence, fainter and lower S/N in *Herschel* $100\ \mu\text{m}$ images. Therefore, we are unable to measure the dust temperature below 20 K. Gordon et al. (2014) analysed the overall dust in the SMC ISM, and estimated the mean SMC dust temperature of below 20 K, hence it is obvious that we cannot analyse such low temperature regions with insufficient S/N.

6.3 Discussion of the dust temperature map for DEMS103 and NGC 346

The combination of high-surface density and low dust temperatures at the location of the stellar clusters bears a striking resemblance to the G 316.75–00.00 ridge in the Milky Way, as seen by Watkins et al. (2019). In the case of G316.75, a high-column density and low-dust temperature filament, containing four embedded O-type stars, is located at the centre of a bipolar HII region, powered by those stars. The photoionising UV radiation from these embedded high-mass stars is inefficient at heating and disrupting gas along the axis of the filament, but can much more easily escape in the perpendicular direction, ionising the surrounding lower-density gas that is exposed to the radiation.

A similar scenario could explain many of the features in the west of NGC 346, such as the presence of the cold, high-density dust ridge surrounded by the ring of warmer and more diffuse dust. The warm dust is associated with the HII region, and has probably been heated by massive stars contained within the clusters embedded within the ridge. This ridge could well be the natal ridge from which the stellar clusters formed, and may itself be the result of compression by the SNR on the north-east side (Sect. 4.1.5). Because the ionised gas mass (and therefore heated dust grains) within it probably accounts for only a small fraction of the total mass, the cold dust dominates the temperature map. The HII region on the south-western side of the ridge explains the free-free radiation seen within the radio and $H\alpha$ data, while on the north-western side of the ridge, the SNR is responsible for the synchrotron radiation. The HII region and the SNR may partially overlap, and the lower gas density on the south-western compared to the south-eastern side may explain the relatively low level of $H\alpha$ emission there.

7 DISCUSSIONS

7.1 SNR detection rate

After examining all 24 SMC SNRs, we report 5 detections and 5 possible detections of associated dust. The MIPS $24\ \mu\text{m}$ is the most effective way to identify the SNRs, produced by various combinations of the dust continuum and lines (Pinheiro Gonçalves et al. 2011). The next most useful band is IRAC $8\ \mu\text{m}$. This band is composed of contributions from synchrotron radiation, [ArII] and [ArIII] lines, with possible H_2 lines, as well as dust emission (Ennis et al. 2006; Reach et al. 2006). MIPS $70\ \mu\text{m}$ is not effective, because of its lower sensitivity and lower angular resolution compared to the 24- and $8\text{-}\mu\text{m}$ bands. In the Galactic survey, the PACS $70\ \mu\text{m}$ was effective at identifying SNRs together with the other *Herschel* bands (Chawner et al. 2019, 2020), however, this band is not available for most of the SMC SNRs.

Amongst five detections, two (SNR J0040.9–7337 and SNR J0127.7–7332) are associated with pulsars/point sources, and only three have detections of a nebulous component associated with SNRs. That leads to a low 13 % detection rate for extended emission in SMC SNRs. Even including possible detections, in total only 6 SNRs have shown extended emission in the infrared.

Far-infrared surveys of SNRs in the Milky Way show that younger (less than 5 000 years) SNRs tend to be more likely to be detected (Chawner et al. 2020). Amongst 5 detected and 5 possible detected sources, only one (SNR J0104.0–7202) has a relatively well determined age (2050 years), so it is very difficult to verify this. With limited number, it is difficult to evaluate if the detection rate has the progenitor mass dependence (Table 2). Either lower ($8\text{--}12.5\ M_\odot$) and relatively higher ($> 21\ M_\odot$) progenitor origins may have a higher detection rate, with little detection in between. However, this is a general tendency of the progenitor mass distribution in the SMC SNRs from Auchettl et al. (2019) rather than dust specific results.

Dokara et al. (2021) reported a spatial anti-correlation between mid-infrared emission and radio emission, however, with a limited sample we did not see such a tendency.

7.2 Dust destruction or something else?

It has been pointed out that the collisionally heated dust model over-predicts dust emission from SNRs (Seok et al. 2013, 2015; Chawner 2020; Priestley et al. 2021). Indeed, our analysis in Sect. 5 may offer this as a possibility: if the $n_{\text{H,ISM}}$, hydrogen density estimated from the HI line is used, the model indeed predicts a much higher brightness than found from those that were measured (case 4). In order to reduce mid-infrared emission, the simplest way is to remove the small grains, leaving only large ($\sim 0.18\ \mu\text{m}$) grains, thus reducing the dust mass by a factor of $\sim 20\%$. That might replicate the situation that small dust grains have been destroyed by SN shocks, while large dust grains survive. Since the mass of dust grains is dominated by large grains, only a small reduction in dust mass can substantially reduce the IR emission. In contrast, when case 1, n_{H} , hydrogen from X-ray EM, is used, the model predicts a reasonable brightness. Uncertainty of the hydrogen density makes it even more challenging to determine if dust grains have been destroyed or not.

An over-prediction of dust emission by the collisionally heated model does exist in all SMC SNRs in general, not limited to SNR J0106.2–7205 (ITK 25) demonstrated in Sect. 5. Table 2 shows the model predicts F'_{24} of $0.4\text{--}7.2\ \text{MJy sterad}^{-1}$, based on $n_{\text{H,ISM}}$

(equivalent to case 2 for SNR J0106.2–7205), meaning that all SNRs could have been detected at $24\ \mu\text{m}$, as the sensitivity limit is $0.3\ \text{MJy sterad}^{-1}$ ($5\ \sigma$), if there is no ISM confusion. In reality, there are only two detections with two more possible detections out of 8 sources. The detection rates seem to be lower, compared to the prediction from the collisionally heated dust model. One possible explanation is that small dust grains have been destroyed, so the $24\ \mu\text{m}$ emission is much lower than predicted. However, we need to be very cautious about this interpretation, as $n_{\text{H,ISM}}$ tends to be a factor of 10 or more higher than n_{H} . It could be possible that the adopted thickness of the SMC for $n_{\text{H,ISM}}$ given by Temim et al. (2015) may be a few factors too small, while the adopted radius is a few factors too large. In such a scenario a combination of the two adjustments, even with some ISM confusion, could potentially resolve the issue of low detection rate. Therefore, at the present time and from our data, there is no conclusive impartial evidence that dust destruction is commonly occurring in SNR shocks.

One concern is that X-ray and dust emission do not always correspond, spatially. Such an example is found in SNR J0052.6–7238 (Fig. 6), which shows dust emission in the north, corresponding to $\text{H}\alpha$, whereas X-ray emission originates in the south with low detections of dust emission. In this case it is probable that the main SNR ejecta and the densest regions of ISM matter do not spatially correspond. Hot plasma emitting from X-ray emission would be missing the dust grains needed to produce collisionally heated dust infrared emissions. If hot plasma is not responsible for dust emission in SNRs, the past dust destruction rate through SNR might have been overestimated.

Slavin et al. (2015) demonstrated that the dust destruction rate reduces substantially, once the shocks change from collisional shocks to radiative shocks. Although there is a dispute over the type of SN involved, the age of SNR J0106.2–7205 is estimated to be 17,600 years (Lopez et al. 2014). At this age it is in general considered to be in the Sedov phase, typically between a few hundred years old to $\sim 10^5$ years old, and the shock is still expected to be collisional. Slavin et al. (2015) argues that at about 6×10^4 years old, the radiative cooling is becoming more significant, but SNR J0106.2–7205 has not yet reached that age. The formal distinction of radiative or non-radiative shocks should be made according to shock velocity (McKee & Hollenbach 1980). Unfortunately, in this case there is no shock velocity estimate present. We therefore assume that this SNR still experiences collisional (and non-radiative) shocks.

In SNR J0106.2–7205 the X-ray and IR emitting regions do not always correspond, while IR emitting regions tend to correspond with $\text{H}\alpha$. That link may be caused by the effect of the density. From eqs. (1) and (3), the dust luminosity approximately follows $L = H \propto n_e T_e^{3/2}$. The infrared emission has a T_e dependence, and T_e is proportional to v_s^2 , where v_s is the shock velocity. On the other hand, $EM \sim n_e^2 \times V$. Assuming that the electron density n_e in the shocks is linearly related to the upstream ISM gas density n_{ISM} , the ISM gas density, hence, n_e may vary by an order of magnitudes in the ISM, while the shock velocity v_s variation within a SNR can be only by a factor of a few, so that ISM gas density could be the major driving factor of infrared brightness. A higher ISM density with a reasonably high velocity shock would therefore cause higher IR emission. X-ray brightness has even stronger dependence on n_e . Assuming that the SPIRE $250\text{-}\mu\text{m}$ image represents ISM density along our line of sight, the ambient ISM density might be higher to the north. Reasonably high ISM density might drive a detectable level of dust emission in the north of the SNR. Also $\text{H}\alpha$ emission is seen in the north of the SNR, and shocks in this region may be radiative shocks, i.e. shocks with H-recombination

lines, weak forbidden lines of low ionised metals and non-thermal X-ray emission (Chevalier & Raymond 1978; Chevalier et al. 1980; Heng 2010). This demonstrates that the hydrogen density is crucial for evaluating infrared brightness, hence, whether dust grains being destroyed or not.

In conclusion, within the given uncertainties, we find no conclusive evidence that SNRs have destroyed local swept-up ISM dust. It has previously been suggested that collisional heating of dust grains may over-predict infrared emission in some SNRs (e.g. Williams et al. 2006; Seok et al. 2015), and indeed, this scenario may be accepted if we assume that small dust grains have been destroyed as in the case of SNR J0052.6–7238. However, we advise caution here when interpreting emission levels. First, electron densities measured from X-ray emission do not necessarily spatially correspond to infrared dust emission. Second, there are uncertainties involved in the size of the SNRs and hydrogen density, even though SMC SNRs have very good distance estimates to date. Considering the uncertainties involved in estimating hydrogen and electron densities, IR emission can be explained without the need to invoke dust destruction.

ACKNOWLEDGEMENTS

We thank Dr. Piere Maggi for very useful input about X-ray emission. *Herschel* is an ESA space observatory with science instruments provided by European-led Principal Investigator consortia and with important participation from NASA. This work is based in part on observations made with the *Spitzer Space Telescope*, which was operated by the Jet Propulsion Laboratory, California Institute of Technology under a contract with NASA. Support for this work was provided by NASA. This publication is based on data acquired with the Atacama Pathfinder Experiment (APEX). APEX is a collaboration between the Max-Planck-Institut für Radioastronomie, the European Southern Observatory, and the Onsala Space Observatory. The ESO program no is 106.218. MM acknowledges support from STFC Ernest Rutherford fellowship (ST/L003597/1), MJB, AB, and RW acknowledge support from European Research Council (ERC) Advanced Grant SNDUST 694520, and HLG acknowledges support from the European Research Council (ERC) in the form of Consolidator Grant COSMICDUST (ERC-2014-CoG-647939). FDP acknowledges support from STFC Consolidated grant.

DATA AVAILABILITY

Spitzer and *Herschel* survey data are available at *Spitzer* Heritage Archive (SHA) (<https://sha.ipac.caltech.edu/applications/Spitzer/SHA/>) and *Herschel* Science Archive (<http://archives.esac.esa.int/hsa/whsa/>)

REFERENCES

- Alan N., Park S., Bilir S., 2019, *ApJ*, 873, 53
- Alsaberi R. Z. E., et al., 2019, *MNRAS*, 486, 2507
- Auchettl K., Lopez L. A., Badenes C., et al. 2019, *ApJ*, 871, 64
- Badenes C., Maoz D., Draine B. T., 2010, *MNRAS*, 407, 1301
- Barlow M. J., et al., 2010, *A&A*, 518, L138
- Bertoldi F., Carilli C. L., Cox P., Fan X., Strauss M. A., Beelen A., Omont A., Zylka R., 2003, *A&A*, 406, L55
- Bica E. L. D., Schmitt H. R., 1995, *ApJS*, 101, 41
- Blair W. P., et al., 2000, *ApJ*, 537, 667

- Bocchio M., Jones A. P., Slavin J. D., 2014, *A&A*, 570, A32
- Bolatto A. D., et al., 2007, *ApJ*, 655, 212
- Borkowski K. J., et al., 2006, *ApJ*, 642, L141
- Bouchet P., et al., 2006, *The Astrophysical Journal*, 650, 212
- Bozzetto L. M., et al., 2017, *ApJS*, 230, 2
- Chawner H., 2020, PhD thesis, School of Physics and Astronomy, <http://orca.cf.ac.uk/138610/>
- Chawner H., et al., 2019, *MNRAS*, 483, 70
- Chawner H., et al., 2020, *MNRAS*, 493, 2706
- Cherchneff I., Dwek E., 2010, *ApJ*, 713, 1
- Chevalier R. A., 1977, *ARA&A*, 15, 175
- Chevalier R. A., Fransson C., 1992, *ApJ*, 395, 540
- Chevalier R. A., Raymond J. C., 1978, *Astrophysical Journal*, 225, L27
- Chevalier R. A., Kirshner R. P., Raymond J. C., 1980, *Astrophysical Journal*, 235, 186
- Coe M. J., Kirk J., 2015, *MNRAS*, 452, 969
- Collaboration P., et al., 2014, *A&A*, 564, A45
- Crawford E. J., Filipovic M. D., McEntaffer R. L., Brantseg T., Heitritter K., Roper Q., Haberl F., Urošević D., 2014, *AJ*, 148, 99
- Danforth C. W., Sankrit R., Blair W. P., Howk J. C., Chu Y.-H., 2003, *ApJ*, 586, 1179
- Davies R. D., Elliott K. H., Meaburn J., 1976, *Memoirs of the Royal Astronomical Society*, 81, 89
- De Looze I., Barlow M. J., Swinyard B. M., Rho J., Gomez H. L., Matsuura M., Wesson R., 2017, *MNRAS*, 465, 3309
- De Looze I., et al., 2019, *MNRAS*, 488, 164
- Decin L., et al., 2012, *A&A*, 548, A113
- Dokara R., et al., 2021, *A&A*
- Dopita M. A., Tuohy I. R., Mathewson D. S., 1981, *ApJ*, 248, L105
- Draine B. T., 2011, *Physics of the Interstellar and Intergalactic Medium*. Princeton
- Draine B. T., Lee H. M., 1984, *ApJ*, 285, 89
- Dwek E., 1998, *ApJ*, 501, 643
- Dwek E., Arendt R. G., 1992, *ARA&A*, 30, 11
- Dwek E., Cherchneff I., 2011, *ApJ*, 727, 63
- Dwek E., Smith R. K., 1996, *ApJ*, 459, 686
- Dwek E., et al., 2008, *ApJ*, 676, 1029
- Ennis J. A., Rudnick L., Reach W. T., Smith J. D., Rho J., DeLaney T. A., Gomez H. L., Kozasa T., 2006, *ApJ*, 652, 376
- Fazio G. G., et al., 2004, *ApJS*, 154, 10
- Ferrara A., Peroux C., 2021, *astro-ph*
- Filipovic M. D., Bohlens T., Reid W., Staveley-Smith L., Jones P. A., Nohejl K., Goldstein G., 2002, *MNRAS*, 335, 1085
- Filipovic M. D., Payne J. L., Reid W., Danforth C. W., Staveley-Smith L., Jones P. A., White G. L., 2005, *MNRAS*, 364, 217
- Filipovic M. D., et al., 2008, *A&A*, 485, 63
- Galliano F., Galametz M., Jones A. P., 2018, *ARA&A*, 56, 673
- Gehrz R. D., 1989, in Allamandola L. J., Tielens A. G. G. M., eds, *Interstellar Dust: Proceedings of the 135th Symposium of the International Astronomical Union*. Kluwer Academic Publishers, Dordrecht, pp 445–
- Gomez H. L., Vlahakis C., Stretch C. M., Dunne L., Eales S. A., Beelen A., Gomez E. L., Edmunds M. G., 2010, *MNRAS: Letters*, 401, L48
- Gomez H. L., et al., 2012a, *MNRAS*, 420, 3557
- Gomez H. L., et al., 2012b, *ApJ*, 760, 96
- Gordon K. D., et al., 2011, *AJ*, 142, 102
- Gordon K. D., et al., 2014, *ApJ*, 797, 85
- Graczyk D., et al., 2020, *ApJ*, 904, 13
- Green D. A., 2009, *Bulletin of the Astronomical Society of India*, 37, 45
- Griffin M. J., et al., 2010, *A&A*, 518, L3
- Gvaramadze V. V., Kniazev A. Y., Oskinova L. M., 2019, *MNRAS*, 485, L6
- Haberl F., Sturm R., Ballet J., et al., 2012, *A&A*, 545, A128
- Hatzidimitriou Cannon D., Hawkins R. D., 1993, *MNRAS*, 261, 873
- Hebbar P. R., Heinke C. O., Ho W. C. G., 2020, *MNRAS*, 491, 1585
- Hendrick S. P., Reynolds S. P., Borkowski K. J., 2005, *ApJ*, 622, L117
- Heng K., 2010, *Publications of the Astronomical Society of Australia*, 27, 23
- Hester J. J., 2008, *ARA&A*, 46, 127
- Heydari-Malayeri M., Selier R., 2010, *A&A*, 517, A39
- Hildebrand R. H., 1983, *Quarterly Journal of the Royal Astronomical Society*, 24, 267
- Hjorth J., Vreeswijk P. M., Gall C., Watson D., 2013, *ApJ*, 768, 173
- Hony S., Gouliermis D. A., of F. G. M. N., 2015, *MNRAS*
- Inoue H., Koyama K., Tanaka Y., 1983, *IAUS*, 101, 535
- Jones A. P., Tielens A. G. G. M., Hollenbach D. J., McKee C. F., 1994, *Astrophysical Journal*, 433, 797
- Jones A. P., Tielens A. G. G. M., Hollenbach D. J., 1996, *ApJ*, 469, 740
- Joseph T. D., Filipovic M. D., Crawford E. J., Bojicic I., 2019, *MNRAS*, 490, 1202
- Katsuda S., Takiwaki T., Tominaga N., Moriya T. J., Nakamura K., 2018, *ApJ*, 863, 127
- Kirchschlager F., Schmidt F. D., Barlow M. J., Fogerty E. L., Bevan A., Priestley F. D., 2019, *MNRAS*, 489, 4465
- Koo B.-C. C., Lee H. G., Moon D. S., the J. L., 2007, *APSJ*, 59, S455
- Koo B.-C. C., Lee J.-J., Jeong I.-G., Seok J. Y., Kim H.-J., 2016, *ApJ*, 821, 1
- Lakicevic M., et al., 2015, *ApJ*, 799, 50
- Laporte N., et al., 2017, *ApJApJ*, 837, L21
- Lee J.-J., Park S., Hughes J. P., Slane P. O., Burrows D. N., 2011, *ApJ*, 731, L8
- Lin D., Webb N. A., Barret D., 2012, *ApJ*, 756, 27
- Long X., Gaetz T. J., Plucinsky P. P., 2020, *ApJ*, 904, 70
- Lopez L. A., Castro D., Slane P. O., Ramirez-Ruiz E., Badenes C., 2014, *ApJ*, 788, 5
- Ludwig B., Sandstrom K., Bolatto A., 2018, in *American Astronomical Society Meeting Abstracts #231*. p. 241.08
- Lundqvist P., et al., 2020, *MNRAS*, 496, 1834
- Maggi P., et al., 2019, *MNRAS*
- Maiolino R., Schneider R., Oliva E., Bianchi S., Ferrara A., Mannucci F., Pedani M., Roca Sogorb M., 2004, *Nature*, 431, 533
- Maitra C., Ballet J., Filipovic M. D., Haberl F., Tiengo A., Grieve K., Roper Q., 2015, *A&A*, 584, A41
- Mathewson D. S., Ford V. L., Dopita M. A., Tuohy I. R., Mills B. Y., Turtle A. J., 1984, *ApJS*, 55, 189
- Mathis J. S., Rumpl W., Nordsieck K. H., 1977, *ApJ*, 217, 425
- Matsuura M., et al., 2009, *MNRAS*, 396, 918
- Matsuura M., et al., 2011, *Science*, 333, 1258
- Matsuura M., Woods P. M., Owen P. J., 2013, *MNRAS*, 429, 2527
- Matsuura M., et al., 2015, *ApJ*, 800, 50
- McKee C. F., Hollenbach D. J., 1980, *ARA&A*, 18, 219
- McLeod A. F., Reiter M., Kuiper R., Klaassen P. D., Evans C. J., 2018, *Nature*, pp 334–336
- Meixner M., et al., 2010, *A&A*, 518, L71
- Meixner M., et al., 2013, *AJ*, 146, 62
- Micelotta E. R., Dwek E., Slavin J. D., 2016, *A&A*, 590, A65
- Micelotta E. R., Matsuura M., Sarangi A., 2018, *Space Science Reviews*, 214, 53
- Michałowski M. J., Watson D., Hjorth J., 2010, *ApJ*, 712, 942
- Morgan H. L., Edmunds M., 2003, *MNRAS*, 343, 427
- Nazé Y., Hartwell J. M., IR S., et al. 2002, *ApJ*
- Nazé Y., Rauw G., Manfroid J., Chu Y.-H., Vreux J. M., 2003a, *A&A*, 408, 171
- Nazé Y., Hartwell J. M., Stevens I. R., Manfroid J., Marchenko S., Corcoran M. F., Moffat A. F. J., Skalkowski G., 2003b, *ApJ*, 586, 983
- Niculescu-Duvaz M., Barlow M. J., Bevan A., Milisavljevic D., De Looze I., 2021, *MNRAS*, 504, 2133
- Nota A., et al., 2006, *ApJ*, 640, L29
- Nozawa T., Kozasa T., Umeda H., Maeda K., Nomoto K., 2003, *ApJ*, 598, 785
- Ossenkopf V., Henning T., Mathis J. S., 1992, *A&A*, 261, 567
- Owen R. A., et al., 2011, *A&A*, 530, A132
- Park S., Hughes J. P., Burrows D. N., Slane P. O., Nousek J. A., Garmire G. P., 2003, *ApJ*, 598, L95
- Payne J. L., White G. L., Filipovic M. D., Pannuti T. G., 2007, *MNRAS*, 376, 1793
- Pellegrini E. W., Oey M. S., Winkler P. F., Points S. D., Smith R. C., Jaskot A. E., Zastrow J., 2012, *ApJ*, 755, 40

- Pilbratt G. L., et al., 2010, *A&A*, 518, L1
- Pinheiro Gonçalves D., Noriega-Crespo A., Paladini R., Martin P. G., Carey S. J., 2011, *AJ*, 142, 47
- Poglitsch A., et al., 2010, *A&A*, 518, L2
- Priestley F. D., Chawner H., Matsuura M., De Looze I., Barlow M. J., Gomez H. L., 2021, *MNRAS*, 500, 2543
- Reach W. T., et al., 2006, *AJ*, 131, 1479
- Reid W., 2014, *MNRAS*, 438, 2642
- Reid W. A., Payne J. L., Filipović M. D., Danforth C. W., Jones P. A., White G. L., Staveley-Smith L., 2006, *MNRAS*, 367, 1379
- Rho J., et al., 2008, *ApJ*, 673, 271
- Rho J., Reach W. T., Tappe A., Hwang U., Slavin J. D., Kozasa T., Dunne L., 2009, *ApJ*, 700, 579
- Rho J., et al., 2018, *MNRAS*, 479, 5101
- Rieke G. H., et al., 2004, *ApJS*, 154, 25
- Roper Q., McEntaffer R. L., DeRoo C., Filipovic M., Wong G. F., Crawford E. J., 2015, *ApJ*, 803, 106
- Rubio M., Contursi A., Lequeux J., Probst R., Barbá R., Boulanger F., Cesarsky D., Maoli R., 2000, *A&A*, 359, 1139
- Sandstrom K. M., Bolatto A. D., Stanimirović S., van Loon J. T., Smith J. D. T., 2009, *ApJ*, 696, 2138
- Sano H., et al., 2019, *ApJ*, 881, 85
- Sarangi A., Cherkneff I., 2015, *A&A*, 575, A95
- Schneider R., Ferrara A., Salvaterra R., 2004, *MNRAS*, 351, 1379
- Seale J. P., et al., 2014, *AJ*, 148, 124
- Seok J. Y., Koo B.-C. C., Onaka T., 2013, *ApJ*, 779, 134
- Seok J. Y., Koo B.-C. C., Hirashita H., 2015, *ApJ*, 807, 100
- Slavin J. D., Dwek E., Jones A. P., 2015, *ApJ*, 803, 7
- Smith C., Leiton R., Pizarro S., 2000, in Alloin Olsen Galaz eds, *ASP Conf Vol. 221, Stars, Gas and Dust in Galaxies: Exploring the Links*. p. 83
- Stanimirović S., Bolatto A. D., Sandstrom K. M., Leroy A. K., Simon J. D., Gaensler B. M., Shah R. Y., Jackson J. M., 2005, *ApJ*, 632, L103
- Sturm R., et al., 2013, *A&A*, 558, A3
- Subramanian S., Subramaniam A., 2009, *A&A*, 496, 399
- Takekoshi T., et al., 2017, *ApJ*, 835, 55
- Takeuchi Y., Yamaguchi H., Tamagawa T., 2016, *PASJ*, 68, S9
- Temim t., Dwek E., 2013, *ApJ*, 774, 8
- Temim t., Dwek E., Tchernyshyov K., Boyer M. L., Meixner M., Gall C., Roman-Duval J., 2015, *ApJ*, 799, 158
- Temim t., Dwek E., Arendt R. G., Borkowski K. J., Reynolds S. P., slane p., Gelfand J. D., Raymond J. C., 2017, *ApJ*, 836, 129
- Temim t., Slane P., Sukhbold T., et al. B. K., 2019, *ApJ*, 878, L19
- Tielens A. G. G. M., 2010, *The Physics and Chemistry of the Interstellar Medium*. Cambridge University Press
- Tuohy I. R., Dopita M. A., Mathewson D. S., Long K. S., Helfand D. J., 1983, in Danziger J., Gorenstein P., eds, *IAUS Vol. 101, Supernova remnants and their X-ray emission*. p. 559
- Ueta T., et al., 2008, *PASJ*, 60, 407
- Van den Bergh S., 2007, *The Galaxies of the Local Group*. Cambridge University Press
- Van der Heyden K. J., Bleeker J. A. M., Kaastra J. S., 2004, *A&A*, 421, 1031
- Vogt F. P. A., Bartlett E. S., Seitzzahl I. R., Dopita M. A., Ghavamian P., Ruitter A. J., Terry J. P., 2018, *Nature Astronomy*, 2, 465
- Watkins E. J., Peretto N., Marsh K. A., Fuller G. A., 2019, *A&A*, 628, A21
- Watson D., Christensen L., Knudsen K. K., Richard J., Gallazzi A., Michałowski M. J., 2015, *Nature*, 519, 327
- Weingartner J. C., Draine B. T., 2001, *ApJ*, 548, 296
- Werner M. W., et al., 2004, *ApJS*, 154, 1
- Wesson R., Barlow M. J., Matsuura M., Ercolano B., 2015, *MNRAS*, 446, 2089
- Williams B. J., et al., 2006, *ApJApJ*, 652, L33
- Xi L., Gaetz T. J., Plucinsky P. P., Hughes J. P., Patnaude D. J., 2019, *ApJ*, 874, 14
- Ye T., Turtle A. J., Kennicutt R. C. J., 1991, *MNRAS*, 249, 722
- Zubko V. G., Mennella V., Colangeli L., Bussoletti E., 1996, *MNRAS*, 282, 1321

APPENDIX A: DESCRIPTION OF INFRARED EMISSION FROM SNRS – NON DETECTIONS AND SNR CANDIDATES

A1 Non detections

A1.1 SNR J0047.2–7308, B0045-73.4, IKT 2: unlikely detection

This SNR is radio bright (panel i of Fig A1), and there are associated circular regions found in $H\alpha$ to the north-west and south-west. There is a filamentary structure in the south-west of the SNR which can be seen in $H\alpha$. Similar structure is found all of the infrared images, however, it is most likely part of a larger ISM structure, as the location of infrared filament is slightly off from $H\alpha$ emitting region. Also, this filament does not stand out in the 3-colour image shown in Fig.A2 – if the filament was part of the SNR, it would tend to stand out in a blue colour against ISM.

There are bright infrared clouds in north-west of the shell, just inside the white circle in Fig A1, however, these clouds are probably not part of the SNR, but associated with molecular clouds or an HII region, as there is no associated emission found in either X-ray or radio images.

A1.2 SNR J0047.5–7306, B0045–73.3: non detection

This SNR was reported in *ROSAT* and *XMM-Newton* X-ray images, with Filipovic et al. (2005) identifying the corresponding radio emission at J004728–730601. Maggi et al. (2019) showed that there are two SNRs in very close proximity (SNR J0047.5–7306 and SNR J0047.2–7308), separated by slightly different X-ray abundance patterns.

In Fig. A3, the $H\alpha$ image (panel h) shows that there are at least two separate nebulae which somewhat overlap. The feature also found in the radio image (panel i). The circle indicates the coordinates and size of the SNR from Filipovic et al. (2005). Filamentary structure is found across the circle in $H\alpha$, and some the structure may extend outside the circle.

Although there is some infrared emission within the white circle of Fig. A3, none of the structure resembles $H\alpha$ ones, leading to its listing as a non-detection. The IR emission is most likely of ISM origin.

A1.3 SNR J0048.4–7319, B0046-73.5, DEM S42E, IKT 4: unlikely detection

In radio, this SNR shows a shell structure, and the corresponding shell is also found in the $H\alpha$ image (Fig. A4). In $H\alpha$, a dense and bright emission nebula is seen to the west. Although this bright nebula dominates the west of the SNR, a combination of MCELS [SII] and $H\alpha$ images shows that the strong sulphur throughout the SNR is not present in the nebula, hence, we deem this bright $H\alpha$ source unlikely to be part of the SNR. The rim of this emission is found in all of the infrared images, some of which have a necklace-like appearance. One of the blobs is the young stellar object candidate S3MC J004815.34-731935.61 (Bolatto et al. 2007). It may be possible that the infrared and $H\alpha$ emission are associated with the young stellar object and HII region.

There is a discrete patch of emission found in north-east of the circle, not only at $8\ \mu\text{m}$ but faintly across the other mid-infrared images. This emission is located between SNR J0048.4–7319 and a cluster of stars Bruck 47 (Bica & Schmitt 1995), both of which are clearly seen in the $H\alpha$ image. It is unclear whether the detected

filaments with two blobs inside at $8\ \mu\text{m}$ belong to SNR, the cluster, or unrelated ISM, even though they are quite strong in sulphur.

There is no clear SNR associated emission detected in the infrared, so this SNR is classified as ‘unlikely detection’.

A1.4 SNR J0049.0–7306: unlikely detection

Hendrick et al. (2005) reported an analysis of *Chandra* spectra, and concluded this to be a core-collapse SNR with O and Ne-rich gas. The Fe/Ne abundance ratio might suggest a progenitor mass in the range of $20\text{--}40\ M_{\odot}$ (Takeuchi et al. 2016). Haberl et al. (2012) listed it as an SNR candidate with faint emission in *XMM-Newton* images, but has not been detected in radio. In optical (Fig. A5 h), there are four point sources, surrounded by some nebulosity. It is difficult to evaluate if this nebulosity is associated with SNR. There is some diffuse emission in the infrared images at 8 and $24\ \mu\text{m}$ but it is not clear if emission is related to the SNR, thus, the SNR is unlikely detected at infrared.

A1.5 SNR J0051.1–7321, DEM S53, B0049-73.6, IKT 6: unlikely detection

This SNR has an estimated age of 14,000 years with a progenitor mass of $13\text{--}15\ M_{\odot}$ (Hendrick et al. 2005; Katsuda et al. 2018). So far, $170\ M_{\odot}$ has been swept up already (Hendrick et al. 2005). Although this SNR has a clear circular shell with an X-ray detection of ejecta inside (Fig. A6), there is little emission corresponding to this feature in the infrared images. Although the $8\ \mu\text{m}$ image shows some faint shell emission on the south-east of the white circle, that part of the shell is relatively faint in the radio image. Since it would be unlikely that only this part of the SNR shell would be detected, we conclude that this must be recorded as an ‘unlikely detection’.

A1.6 SNR J00565–7208: non detection

From *XMM-Newton* observations, Haberl et al. (2012) listed SNR J00565–7208 as an SNR candidate. This SNR has a low-surface brightness in X-ray (Haberl et al. 2012) images. Fig. A7 shows that this SNR candidate is very faint in radio and $H\alpha$. The lack of a clear shape in these reference images makes it difficult to identify the SNR candidate in infrared images.

A1.7 SNR J0057.7–7213: non detection

SNR J0057.7–7213 is listed as an SNR candidate by Haberl et al. (2012), based on the *XMM-Newton* survey of SMC SNRs. Radio emission found next to the X-ray emission (Fig.A8) belongs to SNR J0058.3–7218 (Filipovic et al. 2005), which is displayed in Fig.A9. It is unclear if these are two individual SNRs or if they are linked regions of one single SNR (Haberl et al. 2012). There is no infrared detection, made worse by the bright ISM emission that is overwhelming the region.

There is a bright point source detected in X-ray and radio, as well as at 8 , 24 , and $160\ \mu\text{m}$. This is 2MASS J00573272–7213022, also known as [NHS 2003] 4 from Nazé et al. (2003b). It was initially proposed to be an X-ray binary, due to 40% variabilities in X-ray fluxes (Nazé et al. 2002), but it was later classified as a candidate non-nuclear extragalactic source (Lin et al. 2012). This bright X-ray and infrared source is unlikely to be related to the SNR.

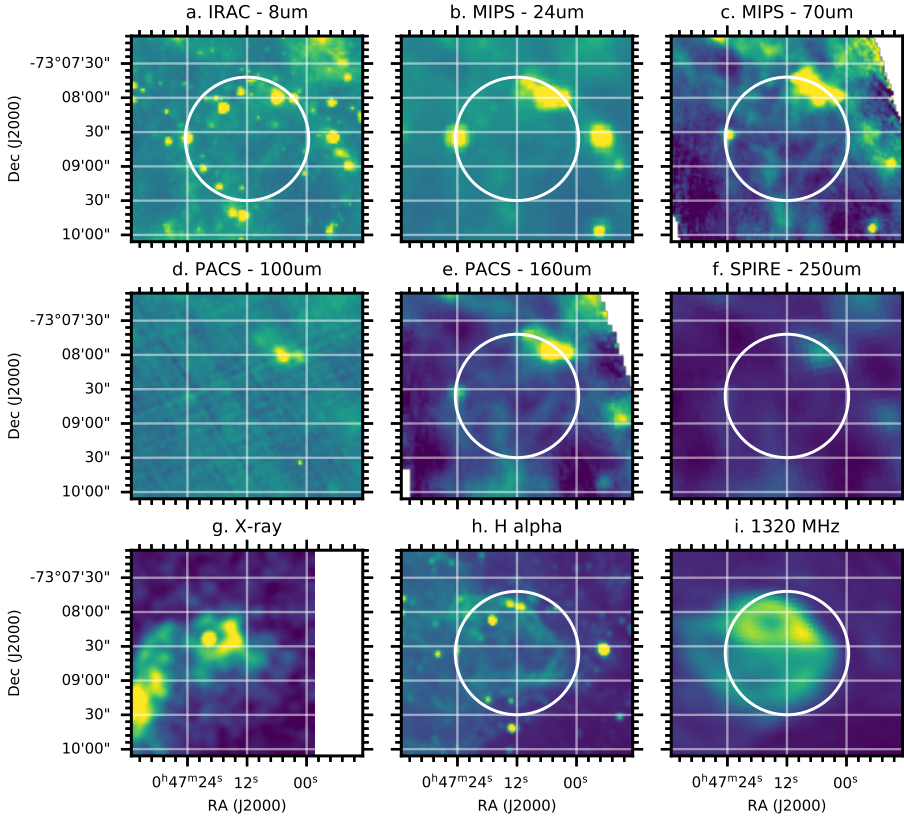


Figure A1. SNR J0047.2–7308, B0045-73.4, IKT 2: unlikely detection. The 70 and 160 μm images are from PACS pointing observations, and the X-ray image is a *Chandra* image in the 0.3–10.0 eV band. It is a bright shell type SNR in radio, but it is faint in $\text{H}\alpha$. Part of the shell might be detected at 8, 70, 160 and possibly 24 μm images near the centre, but it is not totally clear whether they are associated with the SNR or unrelated ISM emission. The bright infrared clouds in north-west of the shell are probably not part of the SNR.

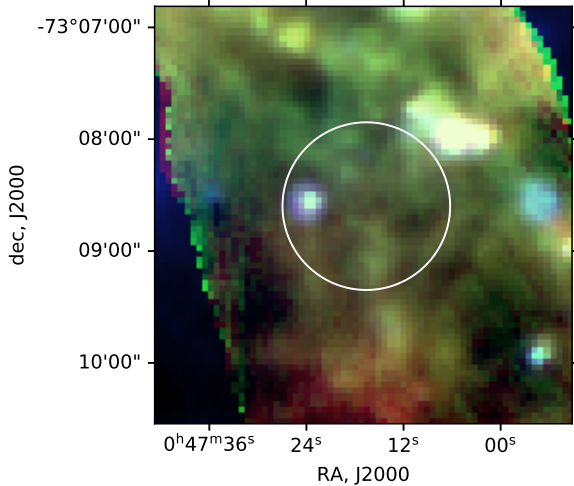


Figure A2. SNR J0047.2–7308, B0045-73.4, IKT 2. - 24, 70 and 160 μm 3-color image. The cirrus within the circle appears to be a continuation of general ISM emission with homogeneous temperatures across the field, rather than dust emission clearly associated with the SNR.

A1.8 SNR J0058.3–7218, B0056-72.5, IKT 16: unlikely detection

SNR J0058.3–7218 is the only pulsar wind nebula known in the SMC (Alsaberi et al. 2019), with an estimated SNR age of 14,700 yrs (Owen et al. 2011). There is a bright point source found in X-ray, which has been identified as emission from the neutron star (Owen

et al. 2011; Maitra et al. 2015). It has also been suggested as a possible AGN (Sturm et al. 2013), however, (Alsaberi et al. 2019) determined it to be a pulsar.

There are two point sources found in $\text{H}\alpha$ (Fig.A9) near the centre: XMMU J005822.1–721759 and XMMU J005820.7–721754. Both of them were listed as AGN candidates before (Sturm et al. 2013) but XMMU J005822.1–721759 was later revised as a pulsar. The source in the east, XMMU J005820.7–721754, is bright in the infrared and it is elongated, but it is probably not associated with the SNR, if it is an AGN candidate.

The $\text{H}\alpha$ image shows bright nebular inside the 1.2 arcmin radius circle (smaller circle in Fig.A9). Although there is some emission on the east side of the inner circle seen in all the infrared images with a point source within, this emission is probably not associated with the SNR, as its morphology does not resemble that of $\text{H}\alpha$.

A1.9 SNR J0100.3–7134, B0058-71.8, DEM S108: non-detection

The radio emission of SNR J0100.3–7134 is bright in the north, while in $\text{H}\alpha$, emission in the southern part, tracing a shell structure, is brighter. Although there is some infrared emission within and surrounding this SNR, the morphology does not resemble radio or $\text{H}\alpha$ (Fig.A10), so this SNR is listed as a non detection.

A1.10 SNR J0103.2–7209, B0101-72.6, IKT 21: unlikely detection

SNR J0103.2–7209 has a well-defined shell structure in radio and $\text{H}\alpha$ (Fig. A11). Observations in [SII] were used to determine a diam-

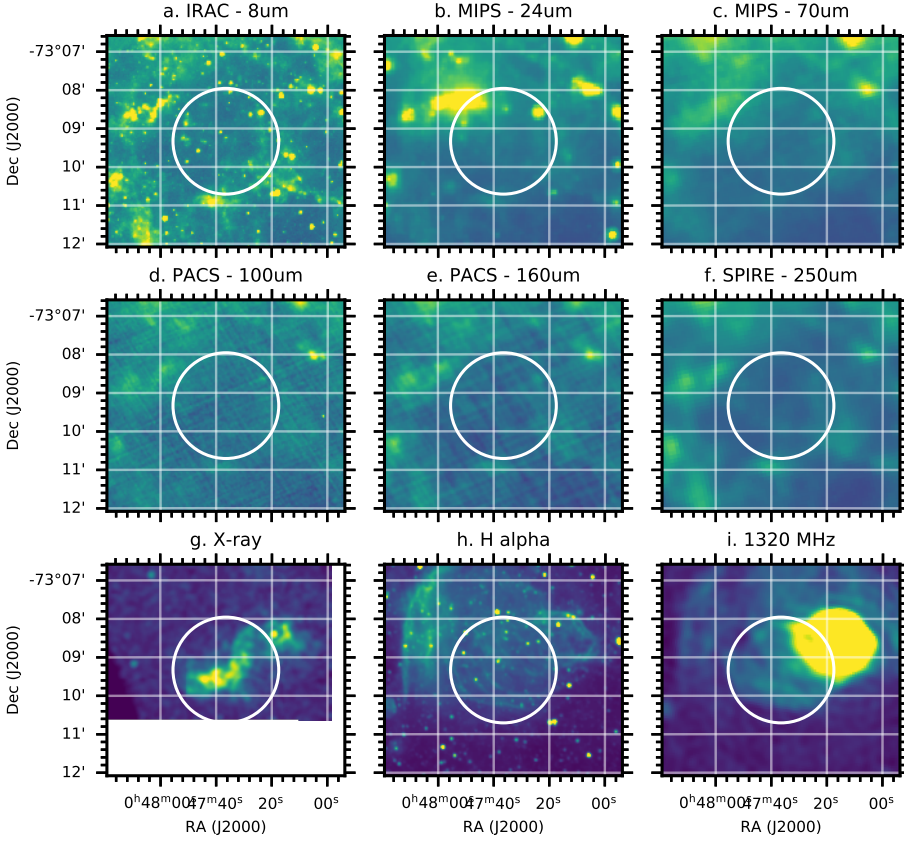


Figure A3. SNR J0047.5–7306, B0045-733 - non-detection. This SNR is located just south of SNR J0047.2–7308.

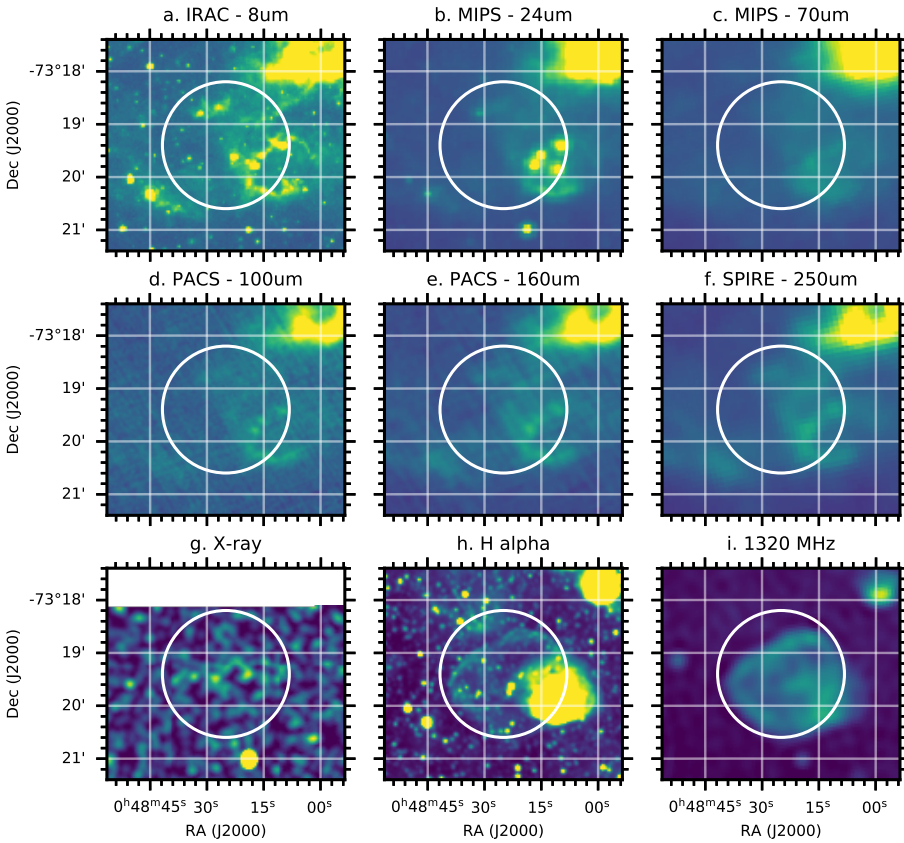


Figure A4. SNR J0048.4–7319, B0046-73.5, DEM S42E, IKT 4: unlikely detection. Panel (g) is a *Chandra* image in the 0.3–10.0 keV band. A structure is found in all the IR images from 8 μm to 250 μm in the south west, but any association with the SNR is not clear. The nebular structure found to the north in the $\text{H}\alpha$, 8 and 24 μm images just inside the white circle is probably not related with SNR.

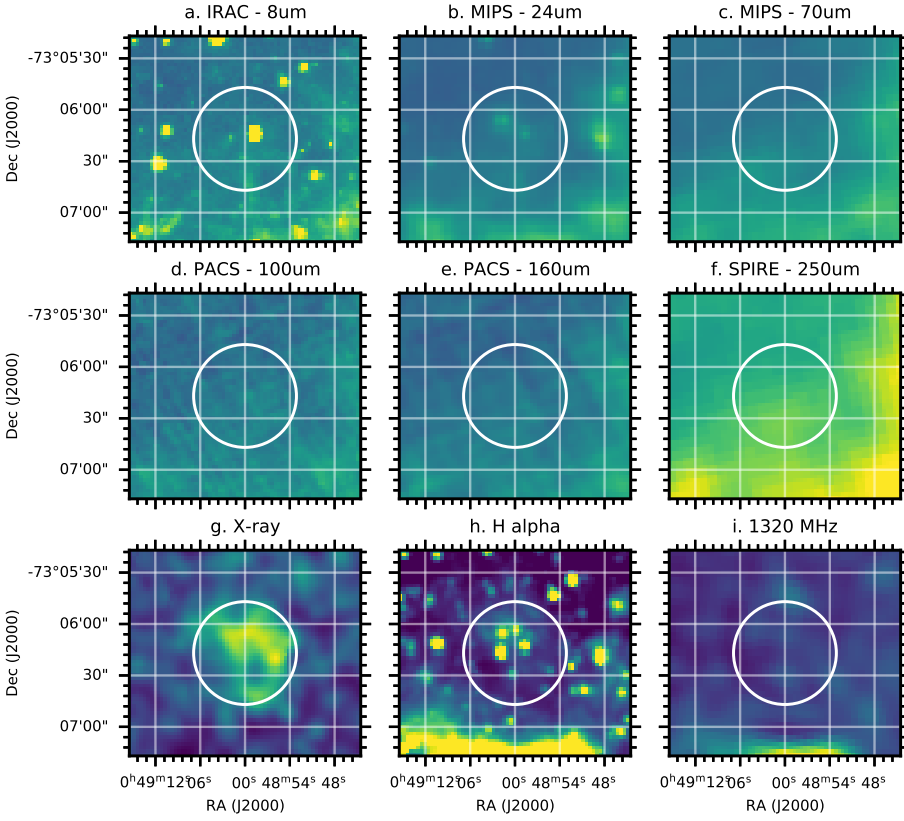


Figure A5. SNR J0049.0–7306: unlikely detection

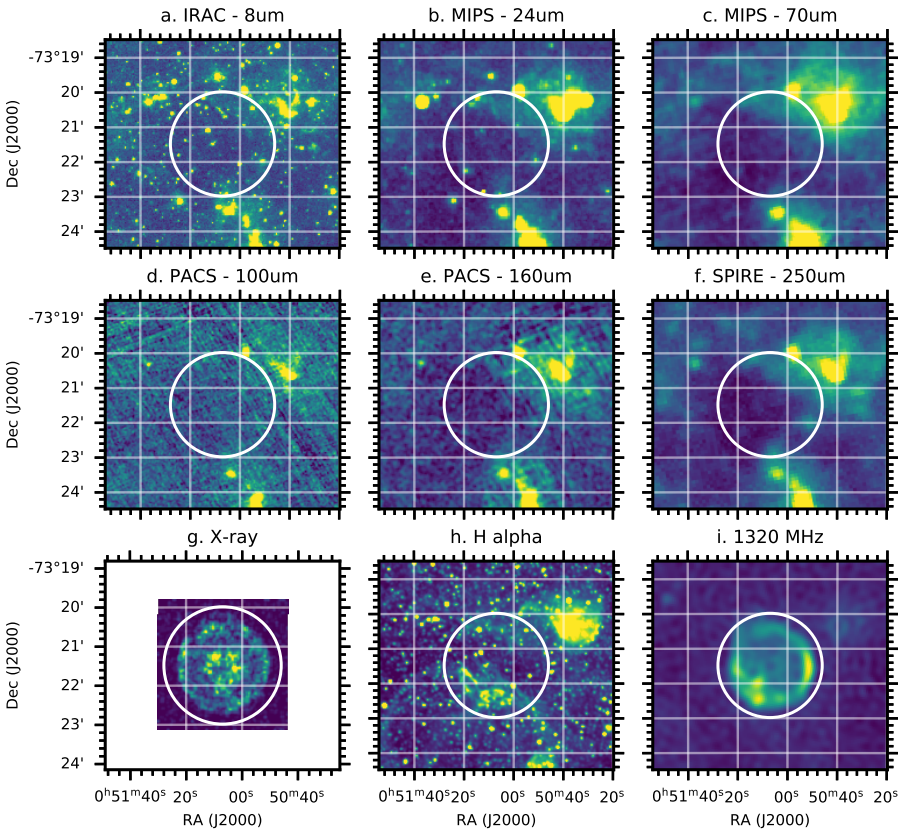


Figure A6. SNR J0051.1–7321, DEM S53, B0049-73.6, IKT 6: non detection. Panel (g) is a *Chandra* image in the 0.3–0.6 keV band.

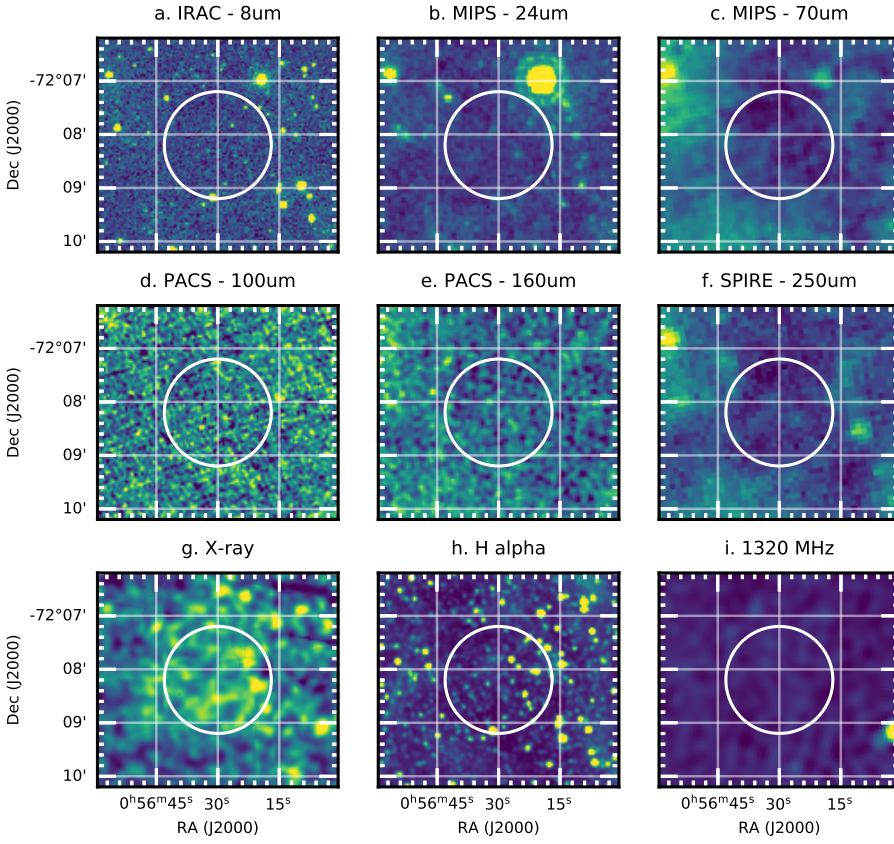


Figure A7. SNR J00565–7208: non detection

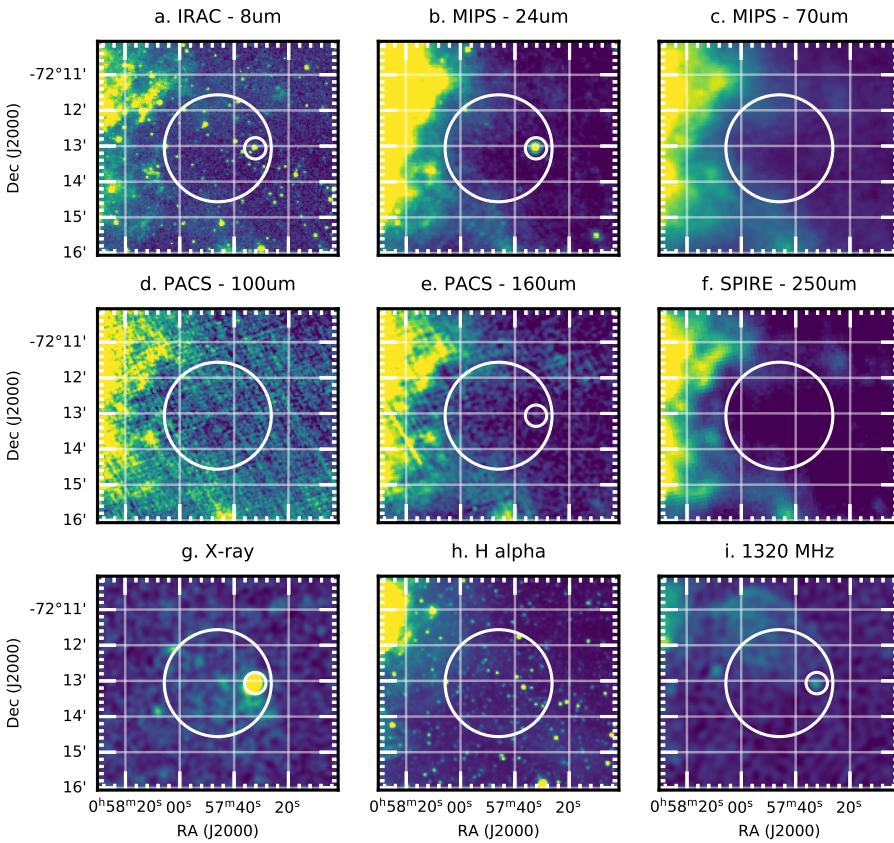


Figure A8. SNR J0057.7–7213: non detection. A bright point source, detected in X-ray, radio and some infrared images is unrelated to the SNR.

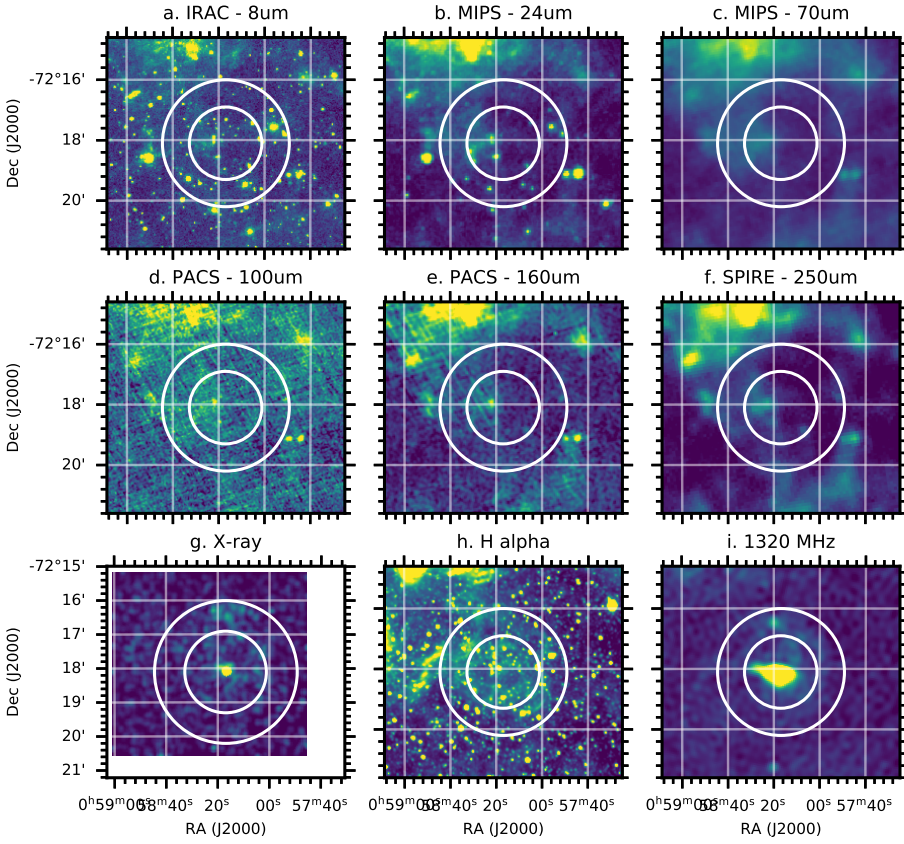


Figure A9. SNR J0058.3–7218, B0056-72.5, IKT 16: unlikely detection. Panel (g) is a *Chandra* image in the 0.58–1.17 keV band.

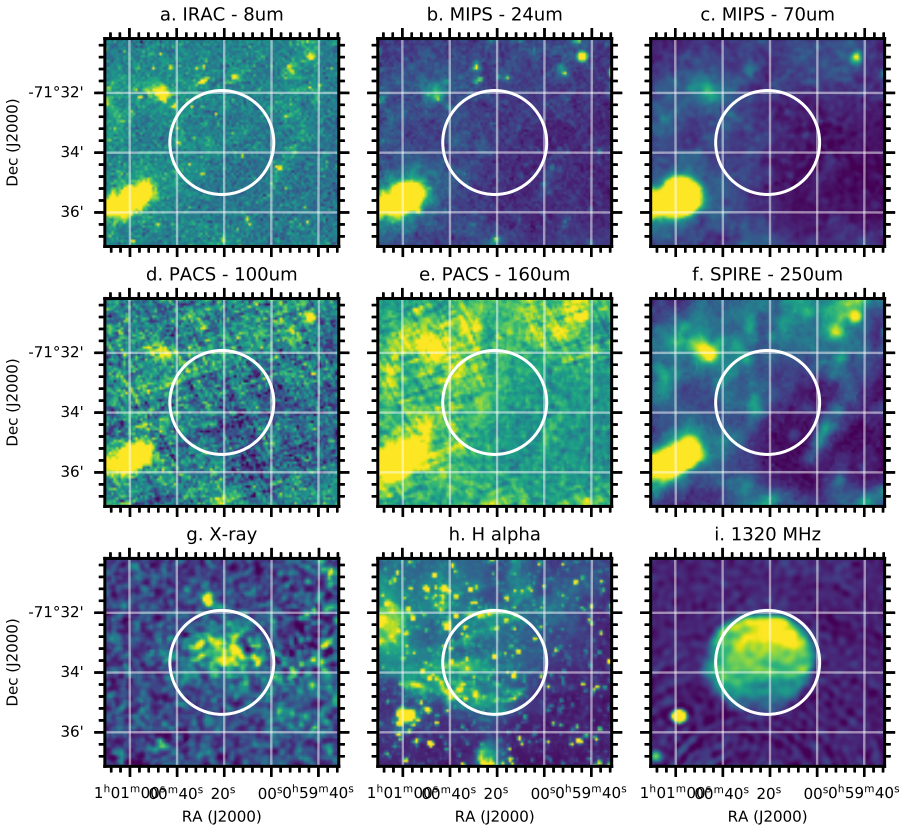


Figure A10. SNR J0100.3–7134, B0058-71.8, DEM S108: non detection.

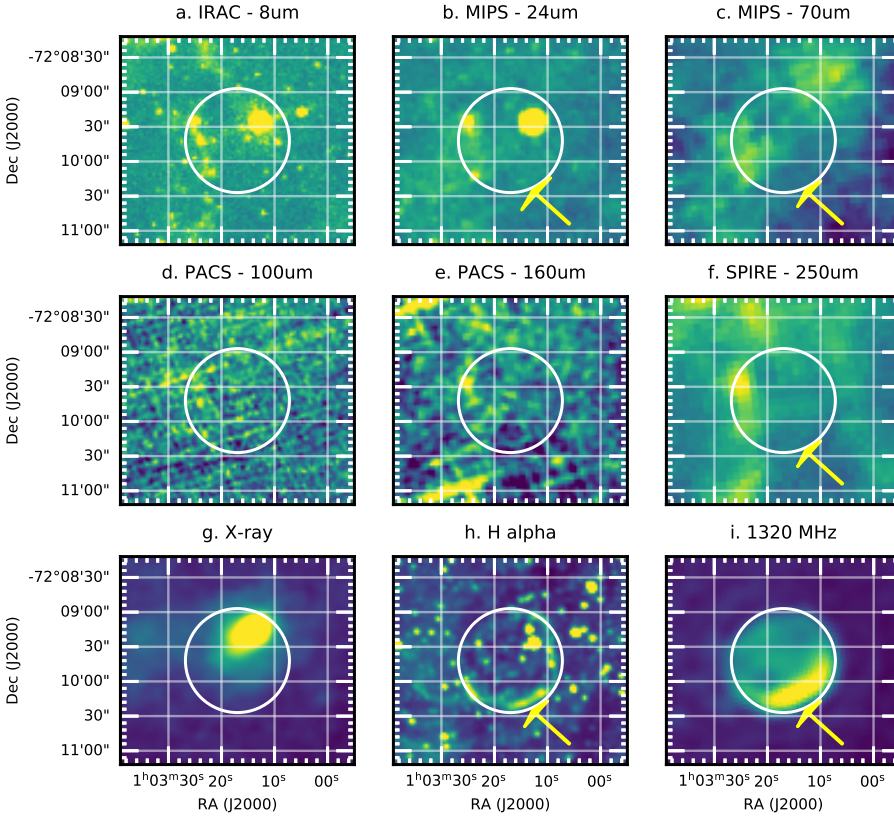


Figure A11. SNR J0103.2–7209, B0101-72.6, IKT 21: unlikely detection.

eter of about 90 arcsec (Mathewson et al. 1984; Maggi et al. 2019). In X-ray, the reported size is much larger at 270 arcsec (Maggi et al. 2019).

$H\alpha$ and radio images both show the brightest part of the rim in the south-west (Fig. A11). This rim may correlate with emission seen in 24 μm and 250 μm , however, due to the limited sensitivity, it is not clearly defined. This SNR is therefore classified as an unlikely detection in infrared.

A1.11 SNR J0105.1–7223, DEM S128, ITK 23: non detection

SNR J0105.1–7223 is the second X-ray brightest SNR in the SMC, and has a core-collapse origin (Van der Heyden et al. 2004; Maggi et al. 2019). Any optical and infrared emission from the SNR, if it exists, is buried within unrelated ISM, which includes the bright region in the south (Fig. A12). This SNR is categorised as a non detection in the infrared.

A1.12 SNR candidate J01065–7242: non detection

This object was relatively recently nominated as a candidate SNR, after detecting radio continuum emission from the ASKAP survey. However, it is yet to be confirmed with an X-ray spectrum (Maggi et al. 2019). Indeed, although the radio image shows a clear spherical shell (Fig A13 i), it is not clearly found in X-ray or $H\alpha$ and there is no sign of infrared emission associated with this SNR.

A1.13 SNR candidate J01097–7318: non detection

SNR candidate J01097–7318 was recognised by a shell-type optical structure, and its high [S II]/ $H\alpha$ ratio in the MCELS survey (Maggi

et al. 2019). It has a clearly defined sphere in the optical (Fig. A14 h). Maggi et al. (2019) stated some issue with the X-ray image, which is also included in this paper (Fig. A14 g). Unfortunately, we don't see any corresponding infrared emission in Fig. A14.

A2 SNR candidates/Non-SNRs?

In this section, we present SNR J0047.8–7317 which had been thought to be SNR, but recent study by Maggi et al. (2019) classified as non SNRs. We display infrared images with possible detection.

A2.1 SNR J0047.8–7317, NS21: possible detection

This source was initially listed as a SNR candidate from radio emission (Filipovic et al. 2002, 2005), with X-ray detections later (Haberl et al. 2012). However, Pellegrini et al. (2012) identified this object (LHA 115-N21) as an HII region, from optical [SII] and [OIII] ratio. Recent radio images by ASKAP did not resolve a shell, hence, considered to be a part of HII region N19 (Maggi et al. 2019).

A point source, corresponding to the radio source, is detected at the centre of this nebula at 24 μm only (Fig. A15). Because it is only one band detection, its identification is undetermined.

An HII region/molecular cloud NGC 267 is located north-east of this SNR, as traced by $H\alpha$ emission, and molecular cloud [RLB 93] SMC-B2 1 (RA 00 47 47.4, Dec –73 16 48) and several young stellar objects are found in between the location of the SNR and NGC 267. These young stellar objects are bright in 8–250 μm .

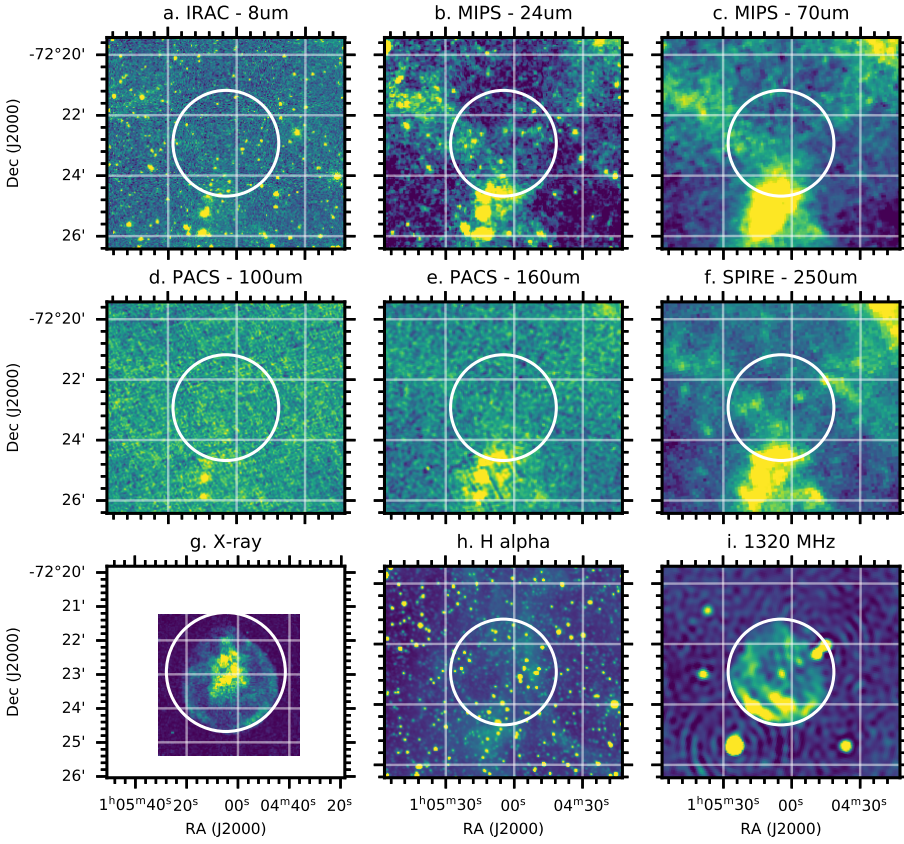


Figure A12. SNR J0105.1–7223, B0103-72.6, DEM S125, IKT 23: non-detection. Panel (g) is a *Chandra* image in the 0.3–10.0 keV band.

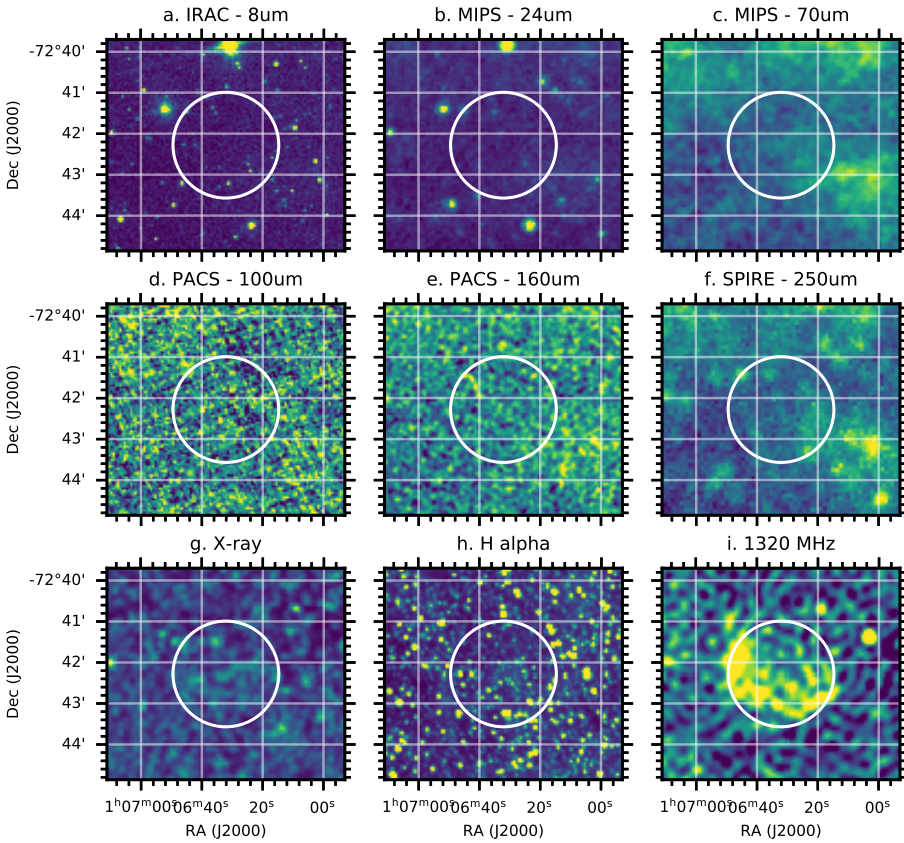


Figure A13. SNR candidate J01065–7242: non detection

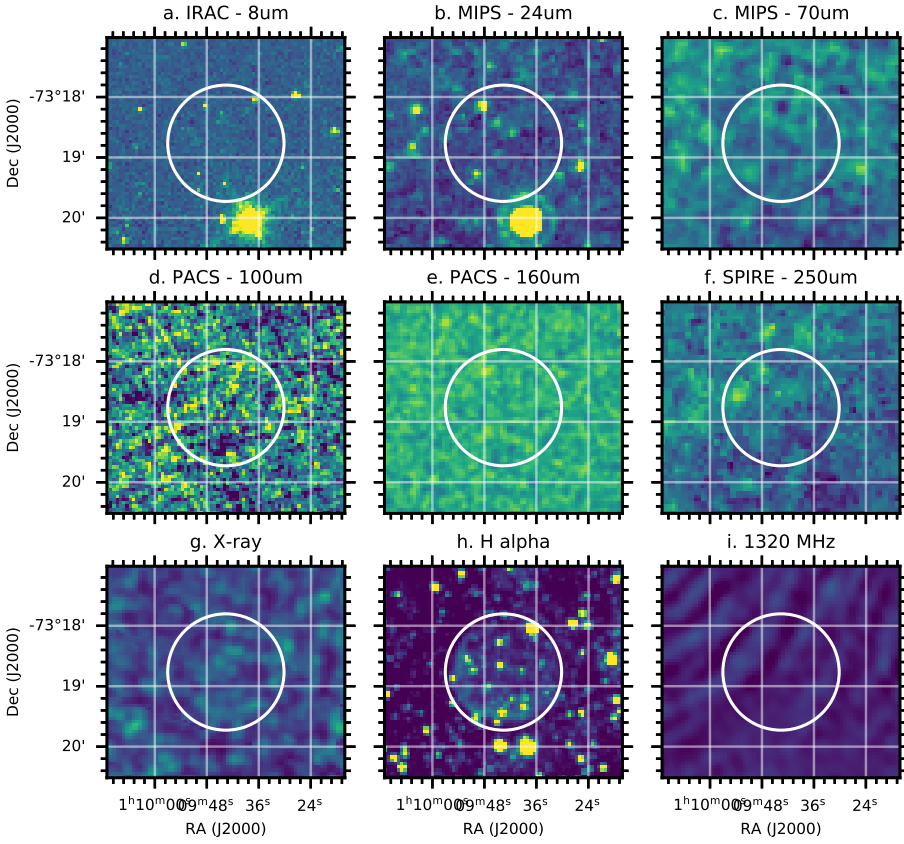


Figure A14. SNR candidate J01097-7318: non-detection

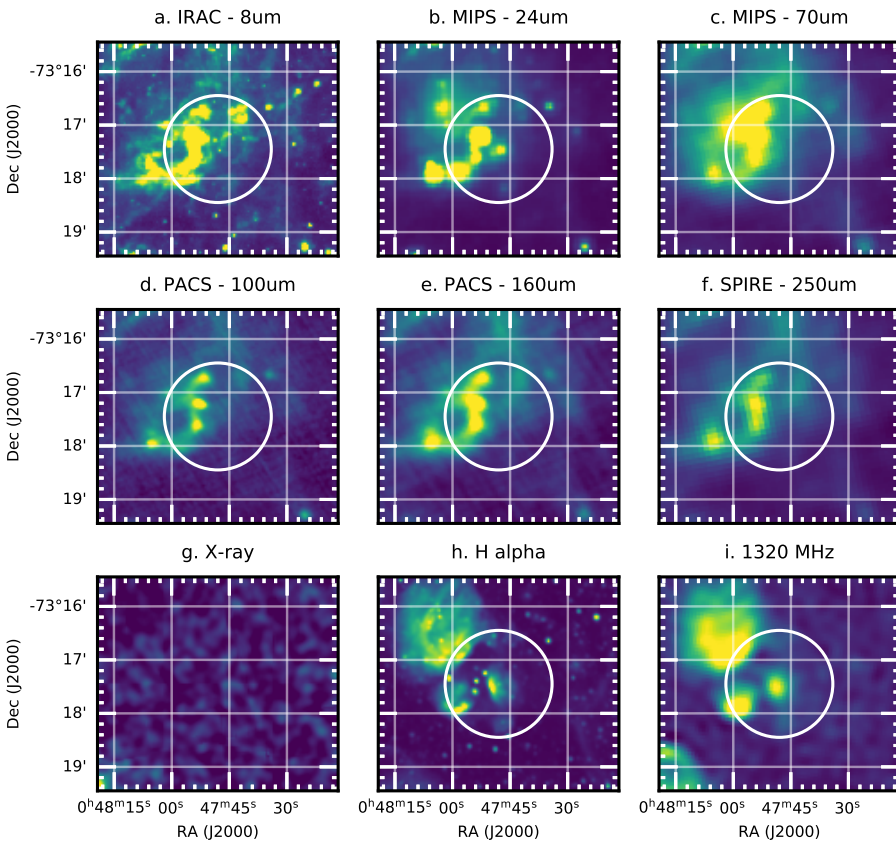


Figure A15. Historically, SNR J0047.8-7317 but recent work found this SNR to be a part of HII region N19. A bright point source is detected at $24 \mu\text{m}$, which has corresponding in $\text{H}\alpha$ and radio emission. Only with a single band detection, it is difficult to evaluate its nature: possible detection.

A2.2 SNR J0051.9–7310, IKT 7: unlikely detection

SNR J0051.9–7310 is a candidate of SNR, reported by *Einstein* X-ray detection (Inoue et al. 1983), however, its identification is still disputed. It could be associated with X-ray Binary, SXP 172 (Coe & Kirk 2015), but could be still core-collapse SNR (Auchettl et al. 2019) It has listed as 97'' diameter in X-ray Badenes et al. (2010) based on on-line source MCSNR, which is no longer available, however, Auchettl et al. (2019) state it as a point source. There is a contradicting information about this potential SNR.

There is no infrared emission associated to this point source Fig.A16. $H\alpha$ image contains so many point sources, so that it is extremely difficult to identify extended emission, if any from SNR. There is also diffuse emission in infrared within the white circle, however, it is difficult to claim that this is associated with possible SNR, so that this SNR is classified as unlikely detection.

A2.3 SNR J0114.0–7317, LHA 115-N 83C: non detection

SNR J0114.0–7317 is listed as SNR candidate by Payne et al. (2007). However, no X-ray emission was detected, and it is likely to be a compact HII region (Maggi et al. 2019).

The infrared image is overwhelmed with nearby star forming region, and can not find any emission from this possible SNR, if any.

This paper has been typeset from a \TeX/L\AA\TeX file prepared by the author.

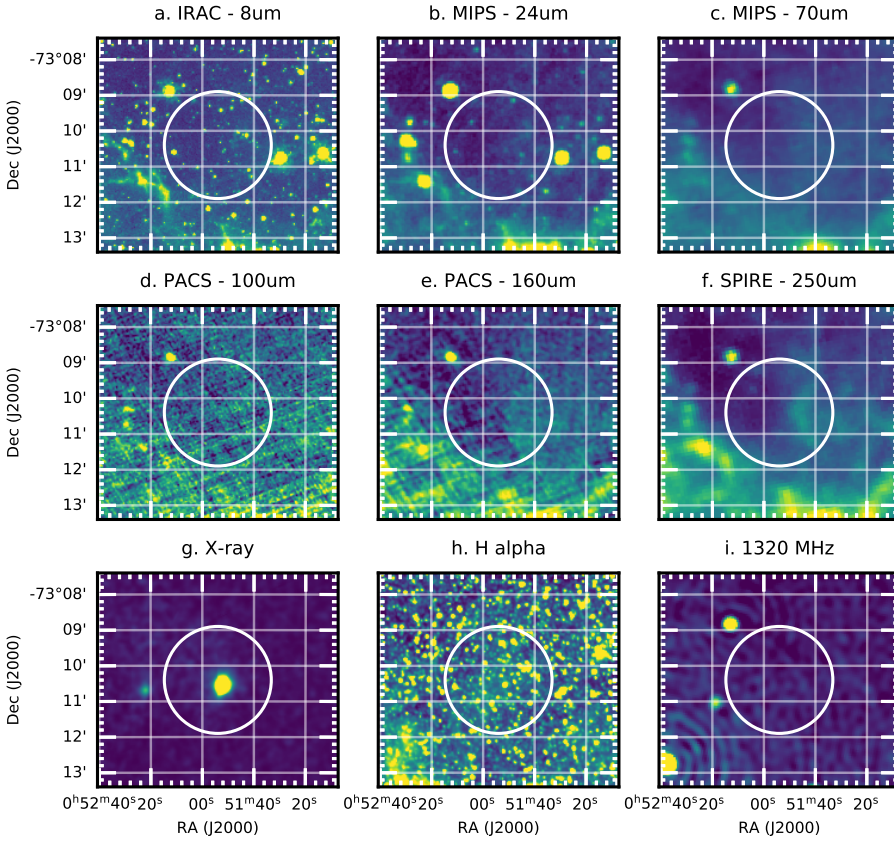


Figure A16. SNR J0051.9–7310, IKT 7: unlike detection.

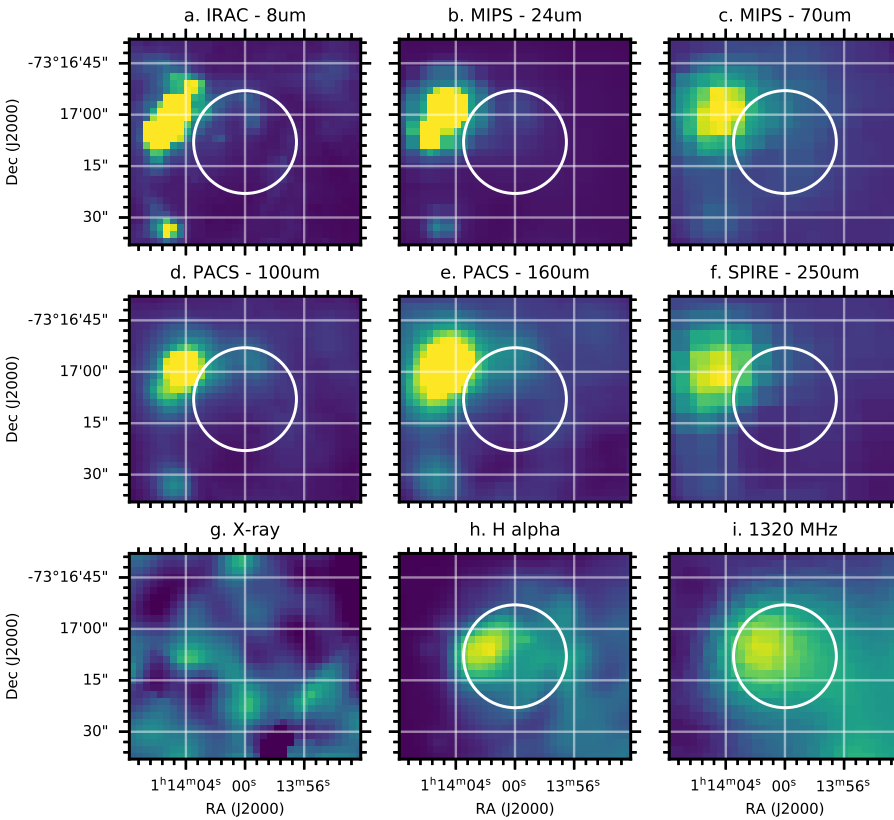


Figure A17. SNR J0114.0–7317, LHA 115-N 83C: no detection.